JOURNAL OF COMPUTATIONAL PHYSICS **128,** 134–164 (1996)
ARTICLE NO. 0200

A High-Order Godunov Method for Multiple Condensed Phases[1]

GREGORY HALE MILLER* AND ELBRIDGE GERRY PUCKETT†

**Department of Geophysical Sciences, University of Chicago, 5734 South Ellis Avenue, Chicago, Illinois 60637; and †Department of Mathematics and Institute of Theoretical Dynamics, University of California, Davis, California 95616*

Received June 20, 1995; revised May 7, 1996

We present a numerical algorithm for computing strong shock waves in problems involving multiple condensed phases. This method is based on a conservative high-order Godunov method in Eulerian form, similar to those that have been used extensively for gas dynamics computations, with an underlying thermodynamic model based on the Mie–Grüneisen equation of state together with a linear Hugoniot. This thermodynamic model is appropriate for a wide variety of nonporous condensed phases. We model multiple phases by constructing an effective single phase in which the density, specific energy, and elastic properties are given by self-consistent averages of the individual phase properties, including their relative abundances. We use a second-order volume-of-fluid interface reconstruction algorithm to decompose the effective single-phase fluxes back into the appropriate individual component phase quantities. We have coupled a two-dimensional operator-split version of this method to an adaptive mesh refinement algorithm and used it to model problems that arise in experimental shock wave geophysics. Computations from this work are presented.

1. INTRODUCTION

We present a numerical method for modeling strong shock waves in condensed matter in which two or more material phases are present. The basis of our algorithm is a second-order Godunov method for approximating solutions of the type originally proposed by Colella [12], Colella and Glaz [14], and Colella and Woodward [17] for the compressible Euler equations for a single material. This methodology is second-order accurate in regions of smooth flow and captures shocks with a minimum of numerical overshoot and dissipation. By itself, this second-order Godunov methodology for a single gas phase has been used extensively to compute unsteady shock reflections in gases and has a demonstrated ability to resolve complex wave interactions in excellent agreement with experiment [20].

Our approach to modeling cells that contain more than one material species is based on an algorithm for modeling two or more gases that is due to Colella, Glaz, and Ferguson (CGF) [15]. In their algorithm the interface between each fluid is tracked with a volume-of-fluid interface tracking algorithm and the equations of motion for a single phase are supplemented with evolution equations for the volume fraction, total energy, and mass density of each phase in the multifluid cells. The resulting system of conservation laws is of hyperbolic type and thus can be solved using a straightforward extension of the second-order Godunov method for a single gas phase. The CGF formulation accounts for the thermodynamic properties of each phase separately, while modeling the pressure and velocity in all cells, including those that contain more than one phase, as single-valued quantities. In particular, given a single uniform pressure acting on a multiphase cell, this algorithm will correctly account for the different compression or expansion that each phase undergoes as a result of that stress. Colella *et al.* [22, 38] have used this algorithm, in conjunction with a second-order volume-of-fluid interface tracking algorithm, to model wave interactions in a medium consisting of two gases. Their results are in excellent agreement with the shock refraction experiments of Abd-el-Fattah and Henderson [1–3] and Jahn [24].

In this paper we describe the extension of the CGF algorithm to materials in condensed phases, i.e., liquids and solids in the hydrostatic limit. In particular, our algorithm is designed to model materials that can be well approximated by the assumption that the Hugoniot is linear in the $U_P - U_S$ plane, where U_S is the shock speed and U_P is the particle velocity. A surprisingly large number of materials are well represented by this assumption, including simple metals and alloys, many woods, polymers, oxides, liquids, and silicates, provided that they are not porous or near a phase transition. Our method is capable of modeling strong compressive waves with large material deformations without ringing (oscillations) and with minimal use of artificial viscosity.

[1] The work of the first author was supported by the National Science Foundation (NSF) under Grant EAR-9304263. The work of the second author was supported by the NSF under Grants DMS-9104472, DMS-9316529, and DMS-9404410 and by the Applied Mathematics subprogram of the Department of Energy's Office of Scientific Computing. Computational support was provided by the National Energy Research Supercomputer Center, the San Diego Supercomputer Center, the National Center for Supercomputing Applications, University of Illinois at Urbana–Champaign, the Pittsburgh Supercomputing Center, and the Institute of Fluid Science at Tohoku University in Sendai, Japan.

0021-9991/96 $18.00

Our work was initially motivated by the need to examine certain edge effect signals that occur in shock wave experiments designed to measure the equation of state (EOS) of geophysical materials [35]. Here we present the results of several computations designed to answer additional questions relevant to that work. We have also studied the accuracy of the method by using it to model high-velocity impact experiments that lead to jetting (e.g., [46]). This latter work appears in [39]. We are especially interested in accurately modeling interpenetration and jetting, particularly as this phenomena appears in geophysical problems.

Given the excellent experimental agreement obtained in the gas dynamics computations cited above we chose to develop a Godunov method to study these problems. Other Godunov methods have been developed to model the types of problems that are of interest to us here. These include CTH [29] and CAVEAT [5] which are based on a solution of the compressible Euler equations in a "Lagrange plus remap" form, rather than the strict Eulerian form upon which our method is based. Moreover, most, if not all, high-order methods that have been developed for modeling condensed phases are based on a discretization of the underlying equations that uses an edge-centered velocity. A careful reading of [49] will show that these methods, which are analogous to the BBC method studied there, have a tendency to smear important features of the flow field such as contact discontinuities. Our method is purely Eulerian, with cell-centered variables, and hence should be less susceptible to diffusive broadening of shock features than Lagrangian plus remap methods [49].

Trangenstein and Colella [44] and Wang *et al.* [47] have developed Godunov methods for modeling elastic–plastic solids. Surveys of numerical methods for modeling impact and penetration problems may be found in Zukas [50] and McGlaun and Yarrington [30]. A capability of the algorithm we describe, not found in most other "hydrocodes," is the incorporation of an Adaptive Mesh Refinement (AMR) algorithm. This feature allows the computational effort to be focused on those areas deemed interesting or error-prone, without reducing the global time step.

The remainder of this paper is organized as follows. In Section 2 we describe the EOS model that we use in our method. In Section 3 we describe the solution of the Riemann problem for materials that satisfy this EOS. In Section 4 we give the details of the second-order Godunov method that we have written to approximate solutions of the Euler equations for materials that obey our EOS. Section 5 contains a description of how we have extended this method in order to model more than one phase of such materials. In Section 6 we give a brief description of those features of the AMR algorithm that are specific to our implementation. In Section 7 we present the results of computations we have made with our method to study questions that arise in the use of shock waves to experimentally measure the EOS of geophysical materials. Finally, in Section 8 we present our conclusions.

2. THE EQUATION OF STATE

A perfectly general thermodynamic description of condensed matter (indeed any matter) is limited only by the conditions of thermodynamic stability that arise from the requirement that the specific internal energy E be a convex function of its natural variables: the specific entropy S and the specific volume $V = 1/\rho$. In terms of the partial derivatives of the energy function, the conditions of stability are as follows:

(i) The heat capacities C_V and C_P must be positive,

$$C_V \equiv \left.\frac{\partial E}{\partial T}\right|_V > 0, \tag{2.1}$$

$$C_P \equiv \left.\frac{\partial H}{\partial T}\right|_P > 0, \tag{2.2}$$

where H is the specific enthalpy, $H = E + PV$.

(ii) The isentropic bulk modulus K_S must be positive,

$$K_S \equiv \left.\frac{\partial P}{\partial \ln \rho}\right|_S > 0. \tag{2.3}$$

(iii) The product of the thermal expansion coefficient,

$$\alpha \equiv -\left.\frac{\partial \ln \rho}{\partial T}\right|_P, \tag{2.4}$$

and the thermodynamic Grüneisen parameter,

$$\gamma \equiv V \left.\frac{\partial P}{\partial E}\right|_V, \tag{2.5}$$

must be nonnegative,

$$\alpha\gamma \geq 0. \tag{2.6}$$

However, these conditions place very weak constraints on the EOS. A perfectly general thermodynamic model may therefore require an arbitrary number of parameters (e.g., [43]), or must be represented in tabular form from which thermodynamic states may be interpolated (e.g., [4, 23]). A perfectly general equation of state is also capable of

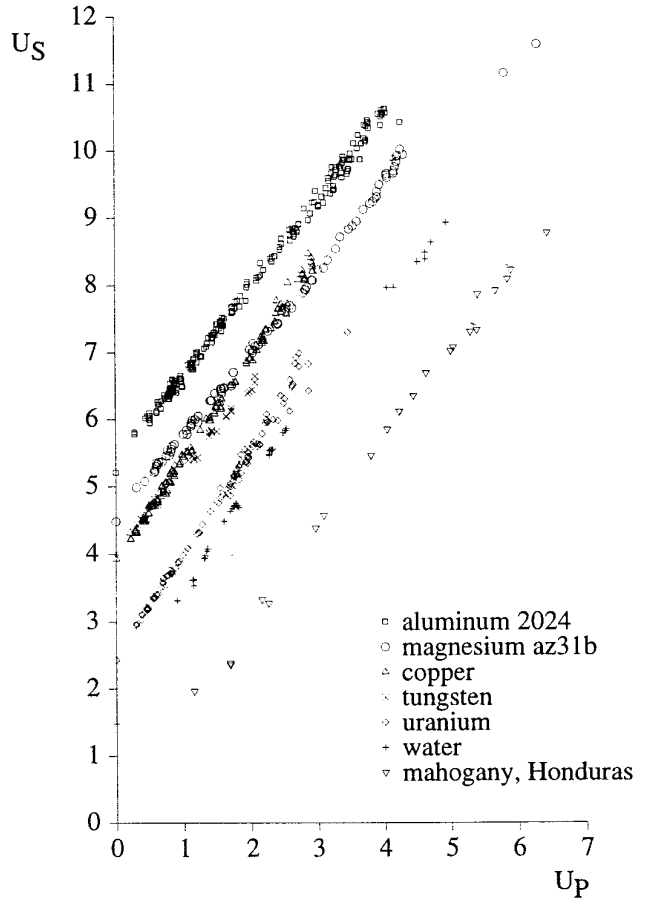

FIG. 1. Representative data for nonporous solids without phase changes from Ref. [28] are well-represented by linear $U_S(U_P)$ Hugoniot equations of state.

exhibiting pathological behavior that leads to complicated and non-unique solutions of the Riemann problem [33].

Despite the latitude afforded by stability requirements, a surprisingly large number of materials have very simple shock equations of state under conditions of single-phase stability [28]. In particular, the shock velocity U_S and the particle velocity U_P are often related by the simple linear Hugoniot equation

$$U_S = c_0 + sU_P \tag{2.7}$$

(e.g., see Fig. 1). It can be shown that the constant c_0 in (2.7) is the bulk sound speed at the centering point (i.e., the thermodynamic state where $U_P \to 0$), and the constant s in (2.7) is related to the isentropic pressure derivative of the isentropic bulk modulus,

$$K_S' \equiv \left.\frac{\partial K_S}{\partial P}\right|_s, \tag{2.8}$$

through

$$s = (K_S' + 1)/4, \tag{2.9}$$

also evaluated at the centering point.

In what follows we assume the validity of the shock EOS (2.7). Materials that are well represented by this assumption include simple metals and alloys (e.g., aluminum, copper, tungsten, tantalum, molybdenum, brass), many woods, polymers (e.g., nylon, Teflon, acrylic, polyethylene), oxides (e.g., periclase, corundum), liquids including water, and silicates (e.g., enstatite, olivine, and molten broadly basaltic compositions) except when they are porous or near phase transitions. Materials that are not well described include fused silica and quartz, which transform to the high-pressure stishovite phase of silica, porous materials, and ideal polytropic gases for which the shock EOS is

$$U_S = \tfrac{1}{4}(\Gamma + 1)U_P + \sqrt{[\tfrac{1}{4}(\Gamma + 1)U_P]^2 + \Gamma P_0 V_0}, \tag{2.10}$$

where $\Gamma = C_P/C_V$ is the adiabatic exponent and the Hugoniot centering point is given by $(V_0, P_0, E_0 = P_0V_0/(\Gamma - 1))$.

These Hugoniot equations of state $U_S(U_P)$ parametrically define thermodynamic shock states through the Rankine–Hugoniot jump relations that express the conservation of mass, momentum, and energy:

$$\rho = \rho_0 \frac{U_S}{U_S - U_P}, \tag{2.11}$$

$$P = P_0 + \rho_0 U_S U_P, \tag{2.12}$$

$$E = E_0 + \frac{1}{2}(P + P_0)(V_0 - V) = \frac{1}{2}U_P^2 + P_0V_0\frac{U_P}{U_S}. \tag{2.13}$$

A single Hugoniot curve, e.g., (2.7) or (2.10), describes only those thermodynamic states (V, P, E) that are accessible by a single shock starting from the thermodynamic state given by the centering point $(V_0 = 1/\rho_0, P_0, E_0)$. A particular centering point is chosen to define the "principal Hugoniot," i.e., the particular (arbitrary) Hugoniot that serves as the backbone for a more general equation of state description. For solids that centering point is usually taken as zero pressure and ideal crystalline density at room temperature (298 K), since those are the conditions from which solid-phase Hugoniots are most often measured. To describe other thermodynamic states, including those accessed by a rarefaction (i.e., a pressure release at constant entropy) from a single shock state, the thermodynamic description offered by the principal Hugoniot EOS must be augmented by additional information.

A thermodynamically rigorous way of describing states off of the Hugoniot is to use a Mie–Grüneisen formalism,

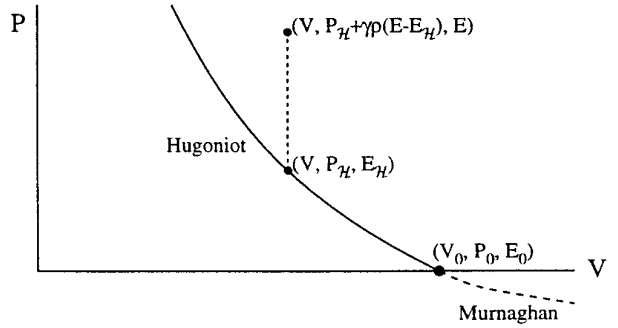

FIG. 2. The Mie–Grüneisen equation of state is constructed from a univariant $P(V)$ reference curve, from which neighboring pressures are determined via (2.15). We use a linear $U_S(U_P)$ Hugoniot for the compression ($V < V_0$) limb of the reference curve and a Murnaghan isentrope for the expansion limb.

$$P(E, V) = P_{\mathscr{H}}(V) + \frac{1}{V}\int_{E_{\mathscr{H}}(V)}^{E} \gamma(V, E)\, dE \qquad (2.14)$$

(see Fig. 2). Here we have assumed that the Hugoniot curve centered at (V_0, P_0, E_0) can be uniquely parameterized by V. In other words, for $V > V_0$, there exist monotonically increasing functions $P_{\mathscr{H}}(V)$ and $E_{\mathscr{H}}(V)$ such that $(V, P_{\mathscr{H}}(V), E_{\mathscr{H}}(V))$ is a unique point on the Hugoniot. The Mie–Grüneisen approach is particularly favored because, at least for states close to the Hugoniot, it is commonly found that the Grüneisen parameter γ depends only on the specific volume, $\gamma = \gamma(V)$, and hence,

$$P(E, V) = P_{\mathscr{H}}(V) + \frac{\gamma(V)}{V}[E - E_{\mathscr{H}}(V)]. \qquad (2.15)$$

The dependence of the Grüneisen parameter on specific volume is often represented by

$$\gamma(V) = \gamma_0 \left(\frac{V}{V_0}\right)^q, \qquad (2.16)$$

where q is a constant that is usually in the range (0, 1). We note that the Grüneisen parameter is positive for most materials and for those materials where it can be negative it is negative only over a limited P–V range. Therefore, when we invoke a model such as (2.16) that precludes a sign change in γ, we will require γ_0 to be positive. When γ is always positive, as implied by (2.16), the energy E is a single-valued function of P and V. Note also that this Grüneisen parameter model is inconsistent with Nernst's postulate that the entropy of systems with nondegenerate ground states is zero at absolute zero of temperature. For consistency with Nernst's postulate the Grüneisen parameter must approach zero at zero temperature [11].

The constitutive equations (2.7) and (2.16), the thermodynamic identity (2.14), and the Rankine–Hugoniot jump relations (2.11–2.13) together give a P–V–E thermodynamic description of many typical condensed phases that is internally consistent and thermodynamically stable over a broad range of P–V–E space near the principal Hugoniot curve. Thus, states accessible by a simple shock process on the principal Hugoniot, and states accessible along a rarefaction from the shock state, are well defined by the equation of state model we use.

We now consider the domain of thermodynamic stability of this equation of state model. We may solve our model equations (2.7), (2.11)–(2.13), (2.15), and (2.16) for the isentropic bulk modulus by writing

$$K_S = \rho \left.\frac{\partial P}{\partial \rho}\right|_S = \rho \left.\frac{\partial P}{\partial \rho}\right|_E + \frac{P}{\rho}\left.\frac{\partial P}{\partial E}\right|_\rho. \qquad (2.17)$$

Evaluated at a principal Hugoniot state, (2.17) becomes

$$K_S = \frac{\gamma}{2}(P - P_0) + K_{\mathscr{H}}\left[1 - \frac{\gamma}{2V}(V_0 - V)\right], \qquad (2.18)$$

where $K_{\mathscr{H}} = dP_{\mathscr{H}}/d \ln \rho$ is the incompressibility taken along the Hugoniot curve. In general, $K_{\mathscr{H}}$ may be written

$$K_{\mathscr{H}} = \frac{U_S}{V_0}(U_S - U_P)\left[\frac{U_S + U_P(dU_S/dU_P)}{U_S - U_P(dU_S/dU_P)}\right], \qquad (2.19)$$

and for a linear material (i.e., obeying (2.7)),

$$K_{\mathscr{H}} = \frac{U_S}{V_0}(U_S - U_P)\left[\frac{c_0 + 2sU_P}{c_0}\right]. \qquad (2.20)$$

This incompressibility will always be positive when $s > 1$; however, the parameter s may be less than 1 for some materials at low pressure. For such materials a linear Hugoniot cannot be extrapolated beyond $U_P = c_0/(1 - s)$ since beyond this limit the particle velocity would exceed the shock velocity, a physical impossibility. Respecting this limit on U_P, the incompressibility (2.20) will be positive for any positive value of s.

We will exclude from consideration materials for which $s < 0$. This limits the shock equation of state to materials whose principal Hugoniots are monotonic and single-valued in pressure. This in turn greatly simplifies the solution of the Riemann problem, discussed in the following section.

Given the positivity of $K_{\mathscr{H}}$, we can see from (2.18) that for $P > P_0$ the isentropic bulk modulus will be negative only when $\gamma > 2V/(V_0 - V)$ (when $P > P_0$ the monotonicity

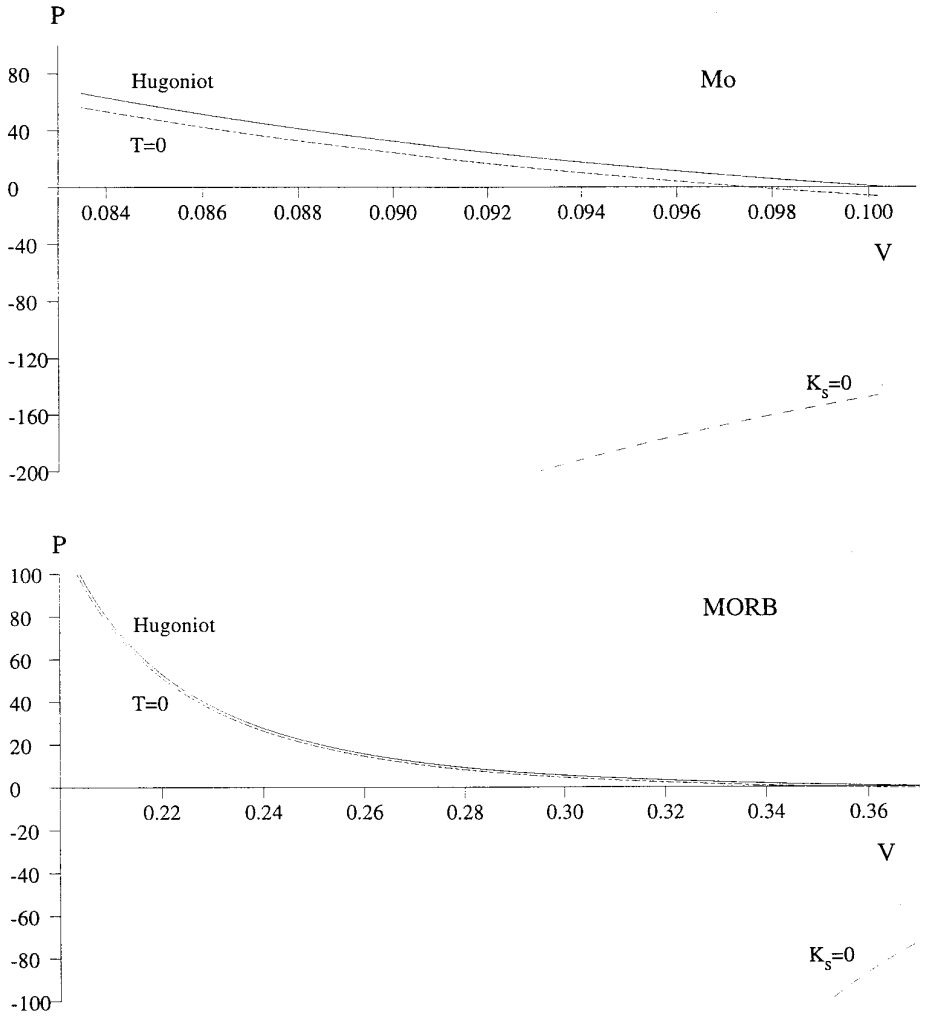

FIG. 3. Pressure–specific volume (P–V) equation of state projections for molybdenum (Mo) and molten midocean ridge basalt (MORB), each at 1400°C. The equation of state parameters are given in Table I. The solid curve is the Hugoniot. The P–V domain of stability is bounded from below by the $K_S = 0$ boundary (dashed). If a thermal model is included, the $T = 0$ absolute zero isotherm (dotted) limits the field of stability. For the equations of state shown here, all super-Hugoniot states are thermodynamically stable. This includes all thermodynamic states accessible by an arbitrary combination of simple shocks and rarefactions.

of the linear Hugoniot requires $V_0 > V$). This condition means that thermodynamic stability is not guaranteed at all points on the principal Hugoniot for arbitrary choice of the parameters γ_0 and q. However, this condition is not particularly restrictive in practice since γ is typically in the range (0.5, 2) and for positive q decreases with compression. Thus this condition of thermodynamic stability is violated only for large γ_0 and for large compression ratios $(V_0/V - 1)$.

The isentropic bulk modulus off of the principal Hugoniot may be determined by direct application of (2.17) to the equation of state (2.15), or by application of a Mie–Grüneisen-type correction to (2.18):

$$\left.\frac{\partial K_S}{\partial E}\right|_\rho = \frac{\gamma(1+\gamma-q)}{V}. \tag{2.21}$$

Here the parameter q is $\partial \ln \gamma / \partial \ln V|_S$, which is compatible with the symbol used in (2.16) but does not necessitate the assumption made there that γ is independent of energy at fixed volume. It is most commonly assumed that $q \leq 1$, and further that $\gamma > 0$, and hence that the isentropic bulk modulus will increase with increasing energy at constant volume. When this is true, increasing energy (equivalently, increasing pressure) will increase the bulk modulus. Thus, for any volume there is some positive pressure for which

the bulk modulus will be positive. Conversely, for any volume there is a pressure (possibly below the Hugoniot) where the bulk modulus will be zero and thus violate (2.3). This low-pressure instability may not limit the overall P–V domain of thermodynamic stability, however, which is also bounded at low pressures by the zero degree isotherm (Fig. 3).

The thermodynamic model presented thus far, i.e., (2.7), (2.11)–(2.13), (2.15), and (2.16), is not complete in that it does not allow determination of temperature, entropy, or free energy of the system. The model must be augmented by additional specification of the heat capacity or thermal expansivity. The computational model presented in this paper does not require such a thermal description. However, for completeness we note that a common assumption such as $C_V = 3k/\text{atom}$, where k is Boltzmann's constant, does not necesssarily satisfy the additional thermodynamic stability requirements. The condition $C_V > 0$ is obviously satisfied by this choice, but the product $\alpha\gamma \equiv \gamma^2 C_V/(VK_S - \gamma^2 C_V T)$ is not guaranteed nonnegative even when $C_V > 0$ and $K_S > 0$. Thus, from the point of view of determining thermodynamic stability, the thermal (C_V) and mechanical (P–V–E) variables cannot be entirely decoupled. Moreover, we note that the stability of a simple shock wave and the uniqueness of the Riemann problem are not guaranteed by a material's thermodynamic stability. Fused silica, for example, is a thermodynamically metastable phase that exhibits shock wave instability over a range of particle velocities.

States of low pressure and high internal energy are problematic with the Mie–Grüneisen EOS description since they necessitate the use of an expanded ($V > V_0$) reference state (Fig. 2). This reference state cannot be the Hugoniot since that would entail negative U_P that are not physically meaningful. For reference volumes greater than V_0 we use a Murnaghan isentropic EOS [37]

$$P = \left(P_0 + \frac{K_{0S}}{K'_{0S}}\right)\left(\frac{\rho}{\rho_0}\right)^{K'_{0S}} - \frac{K_{0S}}{K'_{0S}}. \tag{2.22}$$

The corresponding internal energy state is simply computed from this pressure equation,

$$E = E_0 - \int_{V_0}^{V} P dV. \tag{2.23}$$

The isentropic moduli in the Murnaghan EOS are compatible with the values on the Hugoniot evaluated at its centering point, $K_{0S} = \rho_0 c_0^2$ and $K'_{0S} = 4s - 1$. Thus the Hugoniot and Murnaghan curves are continuous to second order in V.

Finally, for later reference we indicate how the isentropic pressure derivative of the isentropic bulk modulus may be computed:

$$K'_S = \left.\frac{\partial K_S}{\partial P}\right|_S = \left[\rho\frac{\partial P}{\partial \rho} + \rho^2\frac{\partial^2 P}{\partial \rho^2} + \frac{\partial P}{\partial \rho}\frac{\partial P}{\partial E} + 2P\frac{\partial^2 P}{\partial \rho \partial E} - \frac{P}{\rho}\frac{\partial P}{\partial E} + \frac{P}{\rho^2}\left(\frac{\partial P}{\partial E}\right)^2 + \frac{P^2}{\rho^2}\frac{\partial^2 P}{\partial E^2}\right]\frac{1}{K_S}. \tag{2.24}$$

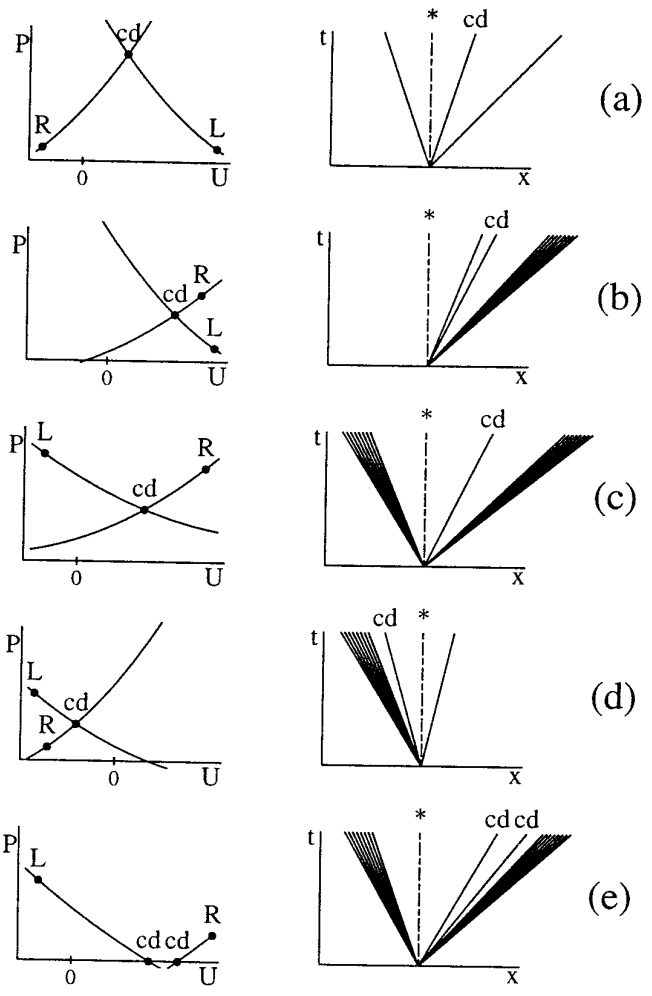

FIG. 4. Schematic pressure–velocity (P–U) wave curve configurations and corresponding time–distance (t–x) characteristics of the five Riemann problem solutions: (a) two shocks, (b) L shock and R rarefaction, (c) two rarefactions, (d) L rarefaction and R shock, and (e) two rarefactions that result in a pressure below the yield strength resulting in spallation. Here "cd" denotes the contact discontinuity and "*" denotes the Eulerian cell-edge characteristic (zero velocity).

3. THE RIEMANN PROBLEM

The Riemann problem is the determination of the wave families that will result from the juxtaposition of two con-

stant states, called here the left and right states and denoted L and R (Fig. 4). The left state has two possible P–U wave curves: one that describes shock states centered at L and one that describes states accessible along a rarefaction from L. The right state has two similarly defined wave curves. The rarefaction limbs of the P–U wave curves are always monotonic, but the shock limbs need not be, and the L and R wave curves might intersect more than once (an odd number of times). With one exception, the intersection of a L and a R wave curve defines the normal stress P^{cd} at the contact discontinuity between the L and R states and the velocity U^{cd} of this interface. This exception occurs when the computed normal stress P^{cd} is negative and greater in magnitude than the strength of either material. Then the solution to the Riemann problem describes a process of cavitation or spallation. In this case the L and R wave curves intersect the wave curve of the interceding vacuum state ($P^{cd} = 0$), and the L-vacuum and R-vacuum interface velocities are distinct (Fig. 4e).

Let us describe the initial constant states by their density, pressure, velocity, and equation of state parameters. We seek new left and right states that satisfy the compatibility conditions of continuity of stress and of velocity at the material interface joining the left and right states. That is, we seek an intersection in the P–U plane of the wave curves emanating from the initial constant states.

The right state, initially given by ρ_R, P_R, E_R, and U_R, might increase its velocity (away from the left state), describing a shock with particle velocity

$$U_R^{cd} = U_R + \sqrt{(P_R^{cd} - P_R)(1/\rho_R - 1/\rho_R^{cd})}, \qquad (3.1)$$

where P_R^{cd} and ρ_R^{cd} satisfy the compatibility conditions and the Rankine–Hugoniot jump relations for a shock centered at (ρ_R, P_R, E_R). Note that (ρ_R, P_R, E_R) may be different from the centering of the principal Hugoniot (ρ_0, P_0, E_0). Alternatively, the right state may decrease its velocity (move toward the left state), describing a rarefaction wave

$$U_R^{cd} = U_R + \int_{P_R}^{P_R^{cd} < P_R} (\rho c)^{-1}\, dP. \qquad (3.2)$$

The possibilities for the left state are analogous, but the sign conventions must be changed to reflect the different directional orientation of that material. The left shock is given by

$$U_L^{cd} = U_L - \sqrt{(P_L^{cd} - P_L)(1/\rho_L - 1/\rho_L^{cd})}, \qquad (3.3)$$

with P_L^{cd} and ρ_L^{cd} lying on the Hugoniot centered at (ρ_L, P_L, and E_L), and the left rarefaction is given by

$$U_L^{cd} = U_L - \int_{P_L}^{P_L^{cd} < P_L} (\rho c)^{-1}\, dP. \qquad (3.4)$$

We have used two methods to solve the Riemann problem with our equation of state. First, we can construct an exact solution to the problem. We accomplish this by writing

$$U_L(P) = U_L - \begin{cases} \displaystyle\int_{P_L}^{P} dP\, \frac{K_S(V_L - V) - \gamma(P - P_L)(V_L - V) + V(P - P_L)}{(2K_S - \gamma(P - P_L))\sqrt{(P - P_L)(V_L - V)}}, & \text{if shock;} \\ \displaystyle\int_{P_L}^{P} dP\, \frac{1}{\sqrt{\rho K_S}}, & \text{if rarefaction.} \end{cases} \qquad (3.5a)$$

$$U_R(P) = U_R + \begin{cases} \displaystyle\int_{P_R}^{P} dP\, \frac{K_S(V_R - V) - \gamma(P - P_R)(V_R - V) + V(P - P_R)}{(2K_S - \gamma(P - P_R))\sqrt{(P - P_R)(V_R - V)}}, & \text{if shock;} \\ \displaystyle\int_{P_R}^{P} dP\, \frac{1}{\sqrt{\rho K_S}}, & \text{if rarefaction.} \end{cases} \qquad (3.5b)$$

In these equations V, γ, and K_S are understood to be functions derivable from the equation of state that vary on the path of integration. Their pressure dependence is different in the Hugoniot and isentropic integrals. The exact solution is found by integrating the L and R wave curves as functions of a common upper limit of integration P until the left-hand sides $U_L(P)$ and $U_R(P)$ are equal. Then their common value is U^{cd} at $P^{cd} = P$, and the thermodynamic variables under these conditions are known from the evaluation of the respective integrands. Additional details are given in the Appendix.

The second approach to solving the Riemann problem is to assume that the shock equation of state, $U_S(U_P)$, centered on the L and R states, is linear. Given our assumed linear Hugoniot equation of state model, this assumption of linearity is strictly true only when the states L and R correspond to the thermodynamic conditions where the principal Hugoniot is centered. Generally, the

shock velocity may be expanded as a power series in particle velocity,

$$U_S = \sum_{i=0}^{\infty} a_i U_P^i, \tag{3.6}$$

where the coefficients a_i may be interpreted thermodynamically,

$$a_0 = \sqrt{K_S/\rho} = c, \tag{3.7a}$$

$$a_1 = (K_S' + 1)/4, \tag{3.7b}$$

$$a_2 = \frac{8K_SK_S'' + (K_S' + 1)(7 + 4\gamma - K_S')}{96c}, \tag{3.7c}$$

etc., where K_S'' is the second isentropic pressure derivative of the isentropic bulk modulus, and where all quantities are evaluated at the centering point; i.e., $U_P \to 0$. Thus, evaluation of K_S and K_S', the isentropic bulk modulus and its isentropic pressure derivative, specifies the two leading coefficients in (3.6) that give a linear approximation to the actual recentered Hugoniot that is second-order in U_P. Pressure, given by

$$P = P_0 + \rho_0 U_S U_P \approx P_0 + \rho_0(cU_P + \tfrac{1}{4}(K_S' + 1)U_P^2), \tag{3.8}$$

will be accurate to second order in U_P.

The rarefaction $dU_P/dP = \pm(\rho c)^{-1}$ may also be expanded in U_P to give

$$P = P_0 + \rho_0\left[cU_P + \frac{(K_S' + 1)}{4}U_P^2 + \frac{K_S''K_S + K_S' + 1}{6c}U_P^3 + \cdots\right]. \tag{3.9}$$

In the pressure–velocity plane the recentered Hugoniot and rarefaction wave curves are equal to second order in U_P. So, to this level of accuracy, we may construct either wave curve as a branch of the same quadratic function $P(U_P)$. With this assumption the solution of the Riemann problem is determined by a simultaneous solution of two quadratic equations:

$$P^{cd} = P_{0R} + \rho_{0R}a_{0R}(U^{cd} - U_R) + \rho_{0R}a_{1R}(U^{cd} - U_R)^2 \tag{3.10}$$

$$P^{cd} = P_{0L} + \rho_{0L}a_{0L}(U_L - U^{cd}) + \rho_{0L}a_{1L}(U_L - U^{cd})^2. \tag{3.11}$$

Here, the right-hand sides are expanded in $(U^{cd} - U_R)$ and $(U_L - U^{cd})$, respectively, to take account of the initial velocities of those states and of their directional orientation.

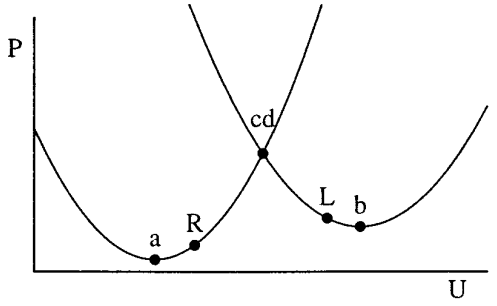

FIG. 5. The Riemann problem approximated with a quadratic $P(U)$ function. Point a on the R wave curve, at $U = U_R - a_{0R}/a_{1R}$, is the point where the isentropic release branch of that wave curve violates the thermodynamic constraint $\rho c > 0$. Point b on the L wave curve, at $U = U_L + a_{0L}/a_{1L}$, is the corresponding point on the release branch of the L curve. The "cd" point indicates the pressure and velocity of the contact discontinuity. In this example both L and R shock waves are predicted.

If we consider recentered Hugoniots whose approximate linear $U_S(U_P)$ relations have positive slope ($a_1 > 0$), then the physical solution to this quadratic equation, if it exists, is always given by

$$U^{cd} = [-b_1 - \sqrt{b_1^2 - 4b_0b_2}]/(2b_2), \tag{3.12}$$

where

$$b_0 = P_L - P_R + \rho_L U_L(a_{0L} + a_{1L}U_L) + \rho_R U_R(a_{0L} - a_{1R}U_R), \tag{3.13a}$$

$$b_1 = -\rho_L(a_{0L} + 2a_{1L}U_L) - \rho_R(a_{0R} - 2a_{1R}U_R), \tag{3.13b}$$

$$b_2 = \rho_L a_{1L} - \rho_R a_{1R}. \tag{3.13c}$$

The other quadratic root is excluded because it is unphysical. It may be shown that the excluded root will be less than $U_R - a_{0R}/2a_{1R}$ or greater than $U_L + a_{0L}/2a_{1L}$. These are the minima of the respective wave curves, and they demark the point on the rarefaction branch of the wave curve where it ceases to be monotonic (Fig. 5). Thus the excluded root lies on a part of the wave curve of either the L or R state where the wave curve is thermodynamically inconsistent with an isentropic rarefaction (thermodynamic consistency requires $dP/dU|_{R/L} = \pm\rho c$; $\rho c > 0$).

The method described here is similar to that of Dukowicz [19] who also employed a quadratic $P(U)$ function. However, we evaluate the coefficients a_0 and a_1 with formulas (3.7a), (3.7b) using the EOS evaluated at the L and R states, which may be significantly different from the Hugoniot centering state, whereas Dukowicz takes the coefficient a_1 to be globally constant. This difference gives our method second-order accuracy in regions of smooth flow

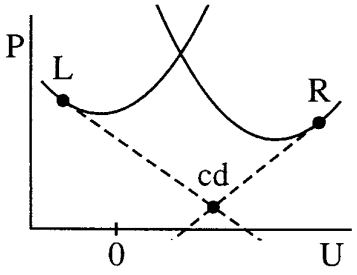

FIG. 6. A failure of the quadratic release branch wave curves to intersect in their domain of thermodynamic stability. To circumvent problems of this sort, which arise at strong rarefactions, the quadratic $P(U)$ wave curve on the rarefaction branch is replaced by a (dashed) line of slope $\rho_R a_{0R}$ or $-\rho_L a_{0L}$ for the R and L wave curves, respectively, when necessary.

even when far from the Hugoniot centering point, where our method is equivalent to Dukowicz's.

We have found that the above quadratic formulation, while robust in the case of smooth flow and arbitrarily strong shocks, fails for strong rarefactions. These occur, for example, when a shock wave collides with a free surface. What happens in this case is that the recentered P–U quadratic may not intersect the $P = 0$ axis (which describes the vacuum state wave curve). In this case there will be no real solutions to the above quadratic equation. To remedy this problem, we make a further simplification: when the solution calls for a rarefaction we replace the constant a_1 with zero (Fig. 6) if this is necessary to make the wave curves intersect. Since thermodynamic stability requires that the coefficient a_0 be positive, the resulting linear P–U wave curve will always intersect the $P = 0$ axis. Of course in making this approximation we have compromised the accuracy of the solver for strong rarefactions. However, this has not proven to be a serious problem as judged by comparison of approximate results with computations conducted with an exact Riemann solver or by comparison to exact solutions in one dimension. The reason our approximate solver works is that rarefactions are intrinsically dispersive. As the wave system expands, the strength of the rarefactions computed by the Riemann solver becomes progressively weaker, the need to linearize the P–U curve lessens, and when required the linear P–U wave curve is more accurate.

We determine whether or not a rarefaction will occur on a given P–U wave curve by taking advantage of the assumed P–U concavity of the quadratic. Define

$$\hat{P}_L = \begin{cases} P_L + \rho_L(U_L - U_R)\,(a_{0L} + a_{1L}(U_L - U_R)) & \text{if } U_L > U_R; \\ P_L + \rho_L a_{0L}(U_L - U_R) & \text{otherwise,} \end{cases} \tag{3.14a}$$

$$\hat{P}_R = \begin{cases} P_R + \rho_R(U_L - U_R)\,(a_{0R} + a_{1R}(U_L - U_R)) & \text{if } U_L > U_R; \\ P_R + \rho_R a_{0R}(U_L - U_R) & \text{otherwise.} \end{cases} \tag{3.14b}$$

Here, $\hat{P}_L$ is the pressure material L would have, given a quadratic P–U wave curve, if its velocity were changed from U_L to U_R; $\hat{P}_R$ is similarly defined. Material L will experience a shock when $P_L > \hat{P}_R$, etc. Thus, when required by a failure of (3.12), the linearization of the P–U wave curve for rarefactions is accomplished by

$$a_{1L} \leftarrow \begin{cases} a_{1L} & \text{when } P_L > \hat{P}_R; \\ 0 & \text{otherwise.} \end{cases} \tag{3.15a}$$

$$a_{1R} \leftarrow \begin{cases} a_{1R} & \text{when } P_R > \hat{P}_L; \\ 0 & \text{otherwise.} \end{cases} \tag{3.15b}$$

In our Godunov method, the Riemann solver must determine not the complete family of waves and characteristics, but the thermodynamic state on the characteristic whose speed is zero. This is the state whose Eulerian coordinate is at the same location as the initial discontinuity between the initial L and R states. We denote this state with the superscript "*". In what follows we shall assume that spallation does not occur.

If the contact discontinuity velocity is greater than zero, $U^{cd} > 0$, then the "*" state lies on a characteristic belonging to the L material. If in addition $P^{cd} > P_L$, then the L solution to the Riemann problem consists of a single recentered shock wave with velocity (according to our equation of state assumptions) $U_S = U_L - a_{0L} + a_{1L}(U^{cd} - U_L)$. If this velocity is positive then the "*" state lies to the left of the shock (* = L). When this velocity is negative the "*" state lies to the right of the shock where the material parameters are determined by the recentered Rankine–Hugoniot jump relations,

$$\rho^* = \rho_L \frac{-a_{0L} + a_{1L}(U^{cd} - U_L)}{U_L - a_{0L} + a_{1L}(U^{cd} - U_L) - U^{cd}}; \qquad \text{L shock} \tag{3.16}$$

$$E^* = E_L + \frac{1}{2}(P_L + P^{cd})\left(\frac{1}{\rho_L} - \frac{1}{\rho_L^*}\right); \qquad \text{L shock.} \tag{3.17}$$

Conversely, when the contact velocity is negative the "*" state samples R material. If a shock occurs, the shock wave velocity $U_S = U_R + a_{0R} + a_{1R}(U^{cd} - U_R)$ determines

whether the "*" state samples unshocked R material or the shocked state. When $U_S > 0$ the "*" state is shocked and the Rankine–Hugoniot jump relations give

$$\rho^* = \rho_R \frac{a_{0R} + a_{1R}(U^{cd} - U_R)}{a_{0R} + a_{1R}(U^{cd} - U_R) + U_R - U^{cd}}; \qquad \text{R shock} \tag{3.18}$$

$$E^* = E_R + \frac{1}{2}(P_R + P^{cd})\left(\frac{1}{\rho_R} - \frac{1}{\rho_R^*}\right); \qquad \text{R shock.} \tag{3.19}$$

A more difficult circumstance than those described above is when $P^{cd} < P_L$, in which case a rarefaction fan will form. The leading edge of the fan travels with speed $U_L - a_{0L}$. The trailing edge of the fan travels with speed $U^{cd} - c_L^{cd}$, where c_L^{cd} is the speed of sound in the L material under the thermodynamic conditions corresponding to the contact discontinuity. An infinite number of characteristics lie between these leading and trailing characteristics.

We compute the sound speed at the contact discontinuity by noting that when the rarefaction wave curve is linear, as assumed above when there is no real solution to the quadratic (3.12), we have

$$\frac{\partial P}{\partial U} = \sqrt{\rho K_S} = \rho c, \text{ a constant.} \tag{3.20}$$

Thus a linear P–U characteristic implies a bulk modulus that varies inversely with density. Integrating this result gives the density of the L state at the contact discontinuity.

$$\rho_L^{cd} = \rho_L \left(1 + \frac{(P_L - P^{cd})}{K_{S,L}}\right)^{-1}. \tag{3.21}$$

In addition, (3.20) gives the speed of sound at the contact discontinuity referenced to the material velocity,

$$c_L^{cd} = a_{0,L} \frac{\rho_L}{\rho_L^{cd}}\ . \tag{3.22}$$

the isentropic $dE = -PdV$ energy integral may also be calculated to give the specific internal energy at the contact discontinuity of the rarefacting material:

$$E_L^{cd} = E_L + \frac{1}{2}\frac{(P^{cd})^2 - P_L^2}{\rho_L K_{S,L}}\ . \tag{3.23}$$

This analysis may also be carried out for a quadratic P–U wave curve. However, as the minimum of the P–U quadratic is approached, the implied thermodynamic properties become unrealistic (the thermodynamic stability condition (2.3) is violated at the minimum). We use the quadratic wave curve to compute U^{cd} when possible, but use the thermodynamic analysis above, which is always based on a linear P–U wave curve. This choice makes our method robust, has little effect on its accuracy, but is otherwise without justification.

The leading and trailing characteristics of the rarefaction fan may be computed with the model given above, as may any characteristic within the fan. However, for computational convenience we interpolate linearly in characteristic velocity to obtain the "*" properties.

In summary, if $U^{cd} > 0$, then the "*" state lies in L material. If a shock occurs and the characteristic associated with the shock is positive, then the "*" state is the original L state: $U^* = U_L$, $P^* = P_L$, $\rho^* = \rho_L$, $E^* = E_L$. If a shock occurs and the characteristic associated with the shock is negative, then the "*" state is the shocked L material state and the Rankine–Hugoniot jump relations apply: $U^* = U^{cd}$, $P^* = P^{cd}$, ρ^* given by (3.16), and E^* given by (3.17). When the "*" state lies in L material but a rarefaction wave exists there, then we interpolate between the leading and trailing characteristics,

$$\begin{pmatrix} U^* \\ P^* \\ \rho^* \\ E^* \end{pmatrix} = (1 - \sigma_L)\begin{pmatrix} U_L \\ P_L \\ \rho_L \\ E_L \end{pmatrix} + \sigma_L \begin{pmatrix} U^{cd} \\ P^{cd} \\ \rho_L \left(1 + \dfrac{(P_L - P^{cd})}{K_{S,L}}\right)^{-1} \\ E_L + \dfrac{1}{2}\dfrac{(P^{cd})^2 - P_L^2}{\rho_L K_{S,L}} \end{pmatrix}, \tag{3.24}$$

where

$$\sigma_L = \min(1, \max(0, \tilde{\sigma}_L)), \tag{3.25a}$$

$$\tilde{\sigma}_L = \frac{a_{0L} - U_L}{a_{0L} - U_L + U^{cd} - c_R^{cd}}\ . \tag{3.25b}$$

Similarly, if $U^{cd} < 0$, then the "*" state lies in R material. If a shock occurs, and its characteristic speed is negative, then the "*" state is the original R state: $U^* = U_R$, $P^* = P_R$, $\rho^* = \rho_R$, $E^* = E_R$. If a shock occurs and its characteristic speed is positive, then the "*" state is given by the Rankine–Hugoniot jump conditions: $U^* = U^{cd}$, $P^* = P^{cd}$,

ρ^* given by (3.18), and E^* given by (3.19). If the "*" state lies in R material but a rarefaction occurs, then

$$\begin{pmatrix} U^* \\ P^* \\ \rho^* \\ E^* \end{pmatrix} = (1 - \sigma_R) \begin{pmatrix} U_R \\ P_R \\ \rho_R \\ E_R \end{pmatrix} + \sigma_R \begin{pmatrix} U^{cd} \\ P^{cd} \\ \rho_R \left(1 + \dfrac{(P_R - P^{cd})}{K_{S,R}}\right)^{-1} \\ E_R + \dfrac{1}{2} \dfrac{(P^{cd})^2 - P_R^2}{\rho_R K_{S,R}} \end{pmatrix}, \tag{3.26}$$

where

$$\sigma_R = \min(1, \max(0, \tilde{\sigma}_R)), \tag{3.27a}$$

$$\tilde{\sigma}_R = \frac{a_{0R} + U_R}{a_{0R} + U_R - U^{cd} - c_R^{cd}}. \tag{3.27b}$$

4. THE SECOND-ORDER GODUNOV METHOD

Our high-order Godunov method for multiple phases is based on some conceptually straightforward modifications of the "standard" single-phase high-order Godunov method (Fig. 7) that has been used extensively to compute problems in gas dynamics. As background to a discussion of these modifications we present a brief summary of the single-phase high-order Godunov method upon which our multiphase algorithm is based.

We begin with the two-dimensional compressible Euler equations written in conservation form,

$$\frac{\partial \mathscr{U}}{\partial t} + \frac{\partial F(\mathscr{U})}{\partial x} + \frac{\partial G(\mathscr{U})}{\partial y} = 0, \tag{4.1}$$

where

$$(\mathscr{U}) = \begin{pmatrix} \rho \\ \rho u \\ \rho v \\ \rho \mathscr{E} \end{pmatrix} \tag{4.2}$$

is the vector of conserved quantities. The corresponding flux vectors in the x and y directions are

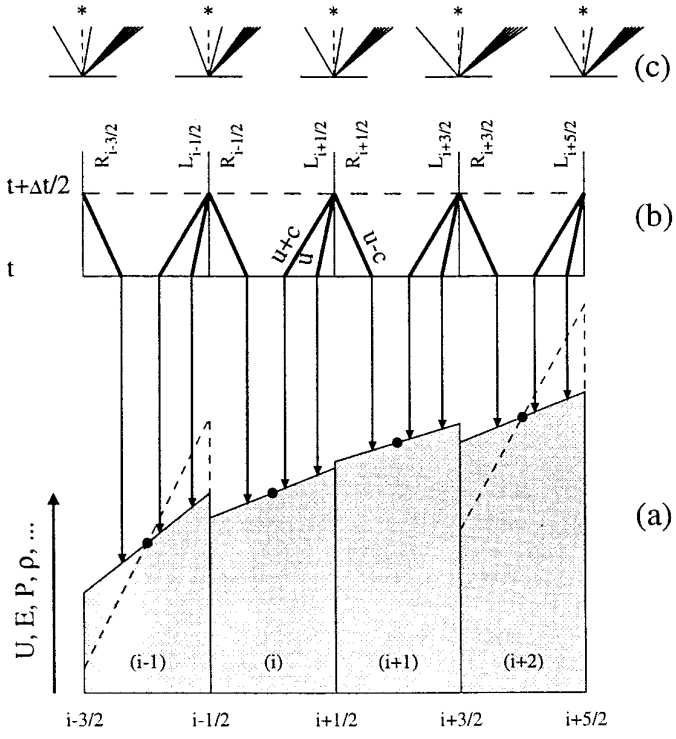

FIG. 7. Schematic representation of a high-order Godunov method. (a) Cell-centered variables (filled dots) are used to construct a central difference approximation to the slope. The resultant distributions (dashed volumes) may be limited to satisfy certain monotonicity constraints (shaded volumes). (b) Upwind characteristic tracing is used to deduce the time-centered cell-edge L and R states that provide the initial data for the Riemann problem. (c) The "*" state of the Riemann problem determines the time-centered fluxes used in the conservative Euler equations.

$$F(\mathscr{U}) = \begin{pmatrix} \rho u \\ \rho u^2 + P \\ \rho u v \\ \rho u \mathscr{E} + uP \end{pmatrix} \tag{4.3}$$

and

$$G(\mathscr{U}) = \begin{pmatrix} \rho v \\ \rho u v \\ \rho v^2 + P \\ \rho v \mathscr{E} + vP \end{pmatrix}, \tag{4.4}$$

where $\mathscr{E} = E + \frac{1}{2}(u^2 + v^2)$ is the total (internal plus kinetic) specific energy. For simplicity we present the algorithm for a Cartesian coordinate system.

We will solve these two-dimensional equations by using a second-order operator splitting technique [42], in which we solve the one-dimensional equations

$$\frac{\partial \mathscr{U}}{\partial t} + \frac{\partial F(\mathscr{U})}{\partial x} = 0 \tag{4.5a}$$

$$\frac{\partial \mathscr{U}}{\partial t} + \frac{\partial G(\mathscr{U})}{\partial y} = 0 \tag{4.5b}$$

in the sequence (4.5a), (4.5b), (4.5b), (4.5a). The time step for each one-dimensional integration is half the time step for the two-dimensional problem.

The essence of a first-order Godunov method [21] is a discretization of (4.5), with the fluxes computed from solutions to the Riemann problem at the cell edges. In other words,

$$\mathscr{U}_i^{n+1} = \mathscr{U}_i^n - \frac{\Delta t}{\Delta x}\left(F(\mathscr{U}_{i+1/2}^{*,n}) - F(\mathscr{U}_{i-1/2}^{*,n})\right), \tag{4.6}$$

where $\mathscr{U}_{i+1/2}^{*,n}$ is the solution to the Riemann problem at coordinate $x_{i+1/2}$ with initial data $\mathscr{U}_{\mathrm{L}}$ and $\mathscr{U}_{\mathrm{R}}$ given by $\mathscr{U}_i^n$ and $\mathscr{U}_{i+1}^n$, respectively.

This method can be made second-order, in both space and time, by computing L and R states from second-order estimates of the value of $\mathscr{U}$ at the cell edge at the half time step $t^{n+1/2} = t^n + \Delta t/2$,

$$\mathscr{U}_i^{n+1} = \mathscr{U}_i^n - \frac{\Delta t}{\Delta x}\left(F(\mathscr{U}_{i+1/2}^{*,n+1/2}) - F(\mathscr{U}_{i-1/2}^{*,n+1/2})\right). \tag{4.7}$$

The time- and edge-centered L and R states are constructed using an upwind characteristic tracing method [14] based on the quasilinear form of (4.1),

$$\frac{\partial \mathscr{Q}}{\partial t} + A\frac{\partial \mathscr{Q}}{\partial x} = 0, \tag{4.8}$$

where

$$(\mathscr{Q}) = \begin{pmatrix} \rho \\ u \\ v \\ P \\ \rho E \end{pmatrix} \tag{4.9}$$

are the variables we choose to trace. The matrix A,

$$A = \begin{pmatrix} u & \rho & 0 & 0 & 0 \\ 0 & u & 0 & 1/\rho & 0 \\ 0 & 0 & u & 0 & 0 \\ 0 & K_S & 0 & u & 0 \\ 0 & \rho H & 0 & 0 & u \end{pmatrix}, \tag{4.10}$$

is evaluated at time n from the cell-centered quantities. The eigenvalue decomposition of A, $A = S\Lambda S^{-1}$, where S is the matrix of right eigenvectors and Λ is the diagonal matrix of eigenvalues, is

$$A = \begin{pmatrix} 1 & 0 & 0 & \rho & \rho \\ 0 & 0 & 0 & -c & c \\ 0 & 1 & 0 & 0 & 0 \\ 0 & 0 & 0 & K_S & K_S \\ 0 & 0 & 1 & \rho H & \rho H \end{pmatrix} \cdot \begin{pmatrix} u & 0 & 0 & 0 & 0 \\ 0 & u & 0 & 0 & 0 \\ 0 & 0 & u & 0 & 0 \\ 0 & 0 & 0 & u-c & 0 \\ 0 & 0 & 0 & 0 & u+c \end{pmatrix} \cdot \begin{pmatrix} 1 & 0 & 0 & -1/c^2 & 0 \\ 0 & 0 & 1 & 0 & 0 \\ 0 & 0 & 0 & -H/c^2 & 1 \\ 0 & -1/(2c) & 0 & 1/(2K_S) & 0 \\ 0 & 1/(2c) & 0 & 1/(2K_S) & 0 \end{pmatrix}. \tag{4.11}$$

The exact solution to the linearized equations (4.8) is

$$\mathscr{Q}_{i\pm1/2}^{n+1/2} = \mathscr{Q}_i^n + \frac{1}{2}(\pm\Delta x I - \Delta t A)\,\mathscr{Q}_x^n, \tag{4.12}$$

where $\mathscr{Q}_x^n$ denotes $\partial\mathscr{Q}/\partial x$ evaluated at time n, but this result includes both upwind and downwind characteristics. To make the solution fully upwind we filter the downwind characteristics from the matrix A, obtaining

$$\mathscr{Q}_{i\pm1/2}^{n+1/2} = \mathscr{Q}_i^n + \frac{1}{2}(\pm\Delta x I - \Delta t S\Lambda^{\pm}S^{-1})\,\mathscr{Q}_x^n, \tag{4.13}$$

$$\Lambda_{ii}^{\pm} = \pm\max(\pm\Lambda_{ii}, 0). \tag{4.14}$$

In other words, in the course of tracing to the right edge of a cell (to $x_{i+1/2} = x_i = \Delta x/2$), only those eigenvalues of A (which is evaluated at x_i) that are positive are retained (Fig. 7b); the negative eigenvalues are set to zero. Conversely, in the course of tracing to the left edge of a cell (to $x_{i-1/2} = x_i - \Delta x/2$) the positive eigenvalues of A are set to zero.

Upwind characteristic tracing requires an estimate of the slopes $\mathscr{Q}_x$ of the cell-centered quantities $\mathscr{Q}$. The slope must be computed with some care to preserve monotonicity and prevent the introduction of spurious oscillations. Van Leer [45] introduced a second-order slope-limiting scheme that is based on a central difference approximation to the cell-centered slope. For each $q \in \mathscr{Q}$,

$$\Delta x|q^{\mathrm{vL}}_{x,i}| = \begin{cases} \min(\frac{1}{2}|q_{i+1} - q_{i-1}|, 2|q_i - q_{i-1}|, 2|q_{i+1} - q_i|) & \\ \qquad \text{if } q_{i-1}, q_i, q_{i+1} \text{ is monotonic;} & (4.15) \\ 0 \qquad \text{otherwise.} & \end{cases}$$

When the sequence q_{i-1}, q_i, q_{i+1} is monotonic (4.15) gives the central difference approximation to the slope, $(q_{i+1} - q_{i-1})/2\Delta x$, possibly reduced so that the extrapolated cell-edge values are guaranteed to lie between the appropriate cell-centered values. Limiting ensures that $q_{i-1/2} = q_i - \Delta x q_x/2$ will fall between q_{i-1} and q_i and that $q_{i+1/2} = q_i + \Delta x q_x/2$ will fall between q_i and q_{i+1}.

Colella [12] modified this slope limiter in two ways. First, the interpolator may be made fourth-order in space by writing

$$q^{\mathrm{4th}}_{x,i} = \frac{2}{3\Delta x}\left(q_{i+1} - \frac{\Delta x}{4} q^{\mathrm{vL}}_{x,i+1} - \frac{\Delta x}{4} q^{\mathrm{vL}}_{x,i-1} - q_{i-1}\right). \quad (4.16)$$

When the van Leer slopes q^{vL}_s are not limited this gives a fourth-order estimate of the slope.

Second, Colella introduced a "flattening" parameter χ to increase dissipation (entropy production) in regions of strong shock waves. In such cases, where abrupt jumps in material properties are expected, a central-difference based slope approximation is not appropriate. Instead, the "flat" first-order Godunov scheme strategy is appropriate. To implement this idea, following Colella and Woodward [17] and Colella [13], we introduce a measure of shock strength

$$z = \frac{|P_{i+1} - P_{i-1}|}{K_{S,i}} \quad (4.17)$$

and obtain a parameter

$$\tilde{\chi}_i = \begin{cases} 0 & \text{if } z > z_1; \\ \dfrac{z_1 - z}{z_1 - z_0} & \text{if } z_1 > z > z_0; \\ 1 & \text{if } z < z_0 \text{ or } u_{i-1} < u_{\mathrm{i}}, \end{cases} \quad (4.18)$$

where z_0 and z_1 are adjustable parameters. In our computations we have used $z_0 = 0.2$ and $z_1 = 0.5$. The parameter $\tilde{\chi}$ will fall in the range [0, 1], and will be less than one only if the pressure jump scaled by the bulk modulus is sufficiently large and the velocity is convergent (i.e., $u_x < 0$). The flattening parameter χ is then given by

$$\chi_i = \begin{cases} \min(\tilde{\chi}_{i-1}, \tilde{\chi}_i) & \text{if } P_{i-1} < P_{i+1}; \\ \min(\tilde{\chi}_i, \tilde{\chi}_{i+1}) & \text{otherwise.} \end{cases} \quad (4.19)$$

In summary, the limited slope we use for the purpose of characteristic tracing is the Colella slope,

$$q^{\mathrm{C}}_{x,i} = \chi_i \min(|q^{\mathrm{4th}}_{x,i}|, |q^{\mathrm{vL}}_{x,i}|)\ \mathrm{sign}(q_{i+1} - q_{i-1}). \quad (4.20)$$

Finally, as is well known (e.g., see Godunov's theorem in [27]), one cannot construct a high-order finite difference solution of equations of the form (4.8) that preserves the monotonicity of the solution. Colella and Woodward [17] found that in Eulerian methods there are circumstances for which no amount of flattening will give sufficient dissipation. A remedy for that problem is that introduction of a small amount of artificial viscosity in regions of convergent flow (i.e., div $u < 0$). Following Colella and Woodward [17] after Lapidus [26], we modify the fluxes (4.3) in regions of convergent flow by

$$F(\mathscr{U})_{i+1/2} \leftarrow F(\mathscr{U})_{i+1/2} + \xi_{i+1/2} \begin{pmatrix} \rho_i - \rho_{i+1} \\ \rho_i u_i - \rho_{i+1} u_{i+1} \\ \rho_i v_i - \rho_{i+1} v_{i+1} \\ \rho_i \mathscr{E}_i - \rho_{i+1} \mathscr{E}_{i+1} \end{pmatrix}, \quad (4.21)$$

$$\xi_{i+1/2} = \max\left(0, -\Delta x \zeta \left[\frac{u_{i+1} - u_i}{\Delta x} + (\nabla_y v)_{i+1/2}\right]\right), \quad (4.22)$$

where

$$(\nabla_y v)_{i+1/2} = \frac{(v_{i+1,j+1} - v_{i+1,j-1}) + (v_{i,j+1} - v_{i,j-1})}{2\Delta y} \quad (4.23)$$

is a central difference approximation to the transverse velocity divergence centered at the $i + 1/2$ cell edge. In (4.22) ζ is a dimensionless adjustable parameter such that when $\zeta = 0$ the artificial viscosity is turned off. In our computations we have used $\zeta = 0.1$. This adds diffusive dissipation when there is a shock, regardless of the orientation of the shock with respect to the direction of integration. However, the inclusion of a transverse velocity gradient in ξ means that artificial viscosity will not be employed at slip lines oblique to the computational grid. Such features can be mistaken for shocks when only the one-dimensional divergence is considered.

In summary, the single-phase high-order Godunov algorithm consists of the following steps: (1) Evaluate the equation of state in each cell using the cell-centered quantities. (2) Compute the flattening parameter χ, and the limited slopes $\mathscr{Q}_x^n$ of the quantities $\mathscr{Q}^n$. (3) At each cell edge, find the time-centered left and right states: $\mathscr{Q}_{\mathrm{L},i+1/2}^{n+1/2}$ by characteristic tracing from cell i and $\mathscr{Q}_{\mathrm{R},i+1/2}^{n+1/2}$ by characteristic tracing from cell $i+1$. (4) Using these L and R states at each cell edge, solve the Riemann problem to determine the time-centered fluxes, $F(\mathscr{U}^{*,n+1/2})$, possibly modified by the addition of an artificial viscosity. (5) Compute the cell centered values of the conserved quantities at the next time step using a conservative update (4.7) with the time-centered fluxes.

5. MULTIPLE PHASES

We are interested in shock wave problems that involve multiple materials, each of which is well approximated by the EOS described in Section 2 above. Our approach to this problem is based on a model developed by Colella *et al.* [15] which has been used extensively to model problems involving multiple phases of polytropic ideal gases (e.g., [22, 38]). The basic idea is to represent the state in each multiphase cell (i.e., a cell that contain more than one phase) as a single phase with internal energy, density, and elastic moduli appropriate to the multiphase composite. The resulting single-phase system is advanced in time by solving for the fluxes of conserved quantities (mass, momentum, and energy), with a high-order accurate Godunov method as summarized above. Those cells that only contain a single phase, say phase 1, and that are neighbored on both sides by cells that also only contain phase 1, are advanced in time using these fluxes. Cells that contain more than one phase before or after the time step are updated with an algorithm that approximates the appropriate fluxes of the single-phase conserved properties (mass and energy of phase 1, mass and energy of phase 2, etc.) from the conserved fluxes of the effective single phase and the volume fractions of each phase in nearby cells. We now describe this algorithm in detail.

5.1. *The Effective Single Phase*

For each cell we specify the following conserved quantities: the mass of each phase, the total energy of each phase, the total normal and transverse momentum of the cell. We additionally specify the volume fractions of each phase (not a conserved quantity), from which the density of each phase may be computed. From this information the amount and thermodynamic state of each phase may be uniquely determined. Specifically, we may compute the pressure P, isentropic bulk modulus K_S, and the isentropic pressure derivative of the isentropic bulk modulus K_S' for each phase from its equation of state.

Let f^α denote the volume fraction of component α and note that

$$\sum_\alpha f^\alpha = 1.$$

We define the mass fraction m^α of component α by

$$m^\alpha = f^\alpha \rho^\alpha / \overline{\rho}, \tag{5.1}$$

where ρ^α is the density of component α, and $\overline{\rho}$, as defined by

$$\overline{\rho} = \sum_\alpha f^\alpha \rho^\alpha, \tag{5.2}$$

is the density of the composite. Similarly we let

$$\overline{E} = \sum_\alpha m^\alpha E^\alpha \tag{5.3}$$

denote the specific internal energy of the composite, where E^α is the specific internal energy of component α. Holding constant the mass of each component, we can write an equation relating the specific volumes $V^\alpha = 1/\rho^\alpha$ to the specific volume $\overline{V}$ of the composite,

$$\overline{V} = \sum_\alpha m^\alpha / \rho^\alpha. \tag{5.4}$$

Differentiating this result with respect to pressure, holding the entropies of each phase individually constant,

$$\left.\frac{\partial \overline{V}}{\partial P}\right|_S = -\sum_\alpha \frac{m^\alpha}{\rho^\alpha} \left.\frac{\partial \ln \rho^\alpha}{\partial P}\right|_S, \tag{5.5}$$

and rearranging gives an expression for the isentropic bulk modulus of the composite:

$$\overline{K}_S = \left(\sum_\alpha f^\alpha / K_S^\alpha \right)^{-1}. \tag{5.6}$$

Differentiation of this result, again separately holding the masses and entropies of each phase constant, gives the isentropic pressure derivative of the isentropic bulk modulus of the composite:

$$\overline{K}_S' = -1 + \overline{K}_S^2 \sum_\alpha \frac{f^\alpha}{K_S^{\alpha 2}} (K_S'^\alpha + 1). \tag{5.7}$$

The justification for holding each phase's entropy individually constant is that thermal equilibrium cannot be maintained on the relevant scales of length and time. The absence of thermal equilibrium can be demonstrated as

follows. The time scale for thermal diffusion is $\tau_{\text{thermal}} \approx L^2/\kappa$, where L is the length scale and κ is the thermal diffusivity. The time scale for acoustic wave propagation, i.e., pressure equalization, is $\tau_{\text{acoustic}} \approx L/c$, where c is the speed of sound. In solids the thermal diffusivity is typically of order 10^{-6} m^2/s, and the sound speed is typically of order 10^3 m/s, and thus the time scales are comparable for length scales on the order of 10^{-9} m, a few orders of magnitude smaller than the smallest cell dimension we have considered.

The effective single-phase quantities $\overline{\rho}$, $\overline{E}$, $\overline{K}_S$, and $\overline{K}'_S$ define the linear approximation to the recentered composite phase Hugoniot (2.7)

$$U_S = \sqrt{\overline{K}_S/\overline{\rho}} + \frac{1}{4}(\overline{K}'_S + 1)U_P, \tag{5.8}$$

from which the approximate Riemann problem may be solved.

A complication arises in the case in which the material is a mixture of one or more condensed phases with a vacuum. Such mixtures occur at the free surface of a body and may be formed by spallation. A homogeneous mixture of matter with vacuum, i.e., a porous material, is perfectly compressible, $K_S = 0$. On rarefaction K_S remains zero, and hence $K'_S = -1$, implying that for a rarefaction the leading coefficients a in (3.6) are $a_0 = a_1 = 0$. If we ignore material strength, then $P = 0$ during compression until the volume fraction f_v of the vacuum is zero. At this point, where pressure first changes on compression, we have $U_S = U_P = 0$ and the density of the composite differs from the initial density of the porous material only by removal of the vacuum volume. The first two terms of the power series expansion (3.6) are thus $a_0 = 0$ and $a_1 = 1/f_v$ on compression. This linear approximation to the power series expansion (3.6) can give a very bad fit to the correct EOS, particularly when f_v is small. To overcome this problem we take $a_0 = 0$ and $a_1 = \min(1/f_v, a'_1)$ for porous multiphase cells, where a'_1 is computed by (3.7b) on a vacuum-free basis.

5.2. *Reconstruction of the Individual Phase Fluxes*

We define a multiphase cell to be a cell that contains a nonzero volume fraction of more than one phase, and we define a multiphase edge to be a cell edge that either:

(a) separates single-phase cells that contain different phases,

(b) bounds a multiphase cell, or

(c) neighbors a cell edge that satisfies criterion (a) or (b).

This definition ensures that cells that can experience a multiphase flux, or that may become multiphase by introduction of a different phase flux, are bounded on each side by a multiphase edge.

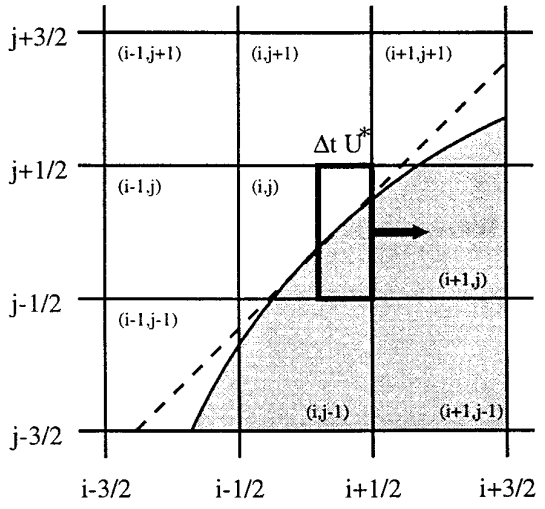

FIG. 8. Schematic representation of the second-order volume-of-fluid interface reconstruction routine.

At each multiphase edge we use a second-order volume-of-fluid interface reconstruction algorithm [25] to determine signed edge-centered individual phase volumes $V^{\alpha\ \text{advected}}_{i+1/2}$ that will be advected across the edge in time step Δt. Let us consider a cell edge, say $(i + 1/2, j)$, for which the Riemann solver has determined a time-centered interface velocity $U^*_{i+1/2,j}$, and let us assume that this velocity is positive (Fig. 8). In time Δt, a volume $\Delta t U^*_{i+1/2,j} A_{i+1/2,j}$ will be advected across the cell edge, where $A_{i+1/2,j}$ is the area of the $(i + 1/2, j)$ edge. That volume, which originates in cell (i, j), may contain more than one phase. The second-order volume-of-fluid strategy we employ seeks a best-fit linear approximation to the interphase boundary and uses that boundary estimate to compute the volume fractions for each phase in the advected volume in the cell upstream of the multiphase edge.

A linear approximation (Fig. 8, dashed line) to the true material interface (Fig. 8, boundary of shaded volume) is found as the solution to a constrained least-squares problem: the function minimized is

$$\sum_{k=i-1}^{i+1} \sum_{l=j-1}^{j+1} (f^{\text{linear}}_{k,l} - f^{\text{actual}}_{k,l})^2,$$

where $f^{\text{actual}}_{k,l}$ are the given volume fractions, $f^{\text{linear}}_{k,l}$ are the volume fractions due to the linear interface with unit normal $\mathbf{n}$, and the (i, j)th cell is the cell upwind of the edge in question. The solution is constrained so that the volume fraction in the center cell due to the line is identical to the actual volume fraction in the center cell

$$f_{i,j}^{\text{linear}}(\mathbf{n}) = f_{i,j}^{\text{actual}}, \tag{5.9}$$

for any $\mathbf{n}$. The intersection of the linear approximation with the advected volume (Fig. 8, bold lines) gives the individual phase fluxes $V_{i+1/2}^{\alpha,\text{advected}}$ whose sum is $U^* \Delta t$. This diagram illustrates a two-phase situation. Multiple-phase volumes are solved by applying this method $N-1$ times for N phases. Each application represents the system as two phases: the phase of interest and everything else.

5.3. *Self-Consistent Multiphase Dynamics*

The equations that express conservation of mass, momentum, and energy are

$$\frac{\partial(f^\alpha \rho^\rho)}{\partial t} + \frac{\partial(f^\alpha \rho^\alpha u)}{\partial x} = 0, \tag{5.10}$$

$$\frac{\partial(\rho u)}{\partial t} + \frac{\partial(\rho u^2 + P)}{\partial x} = 0, \tag{5.11}$$

$$\frac{\partial(\rho v)}{\partial t} + \frac{\partial(\rho v u)}{\partial x} = 0, \tag{5.12}$$

$$\frac{\partial(\rho \mathscr{E})}{\partial t} + \frac{\partial(\rho \mathscr{E} u + P u)}{\partial x} = 0. \tag{5.13}$$

Equations for the evolution of volume fractions f^α and the individual phase specific energies $\mathscr{E}^\alpha$ must take into account the constraints $\Sigma_\alpha f^\alpha = 1$ and $\Sigma_\alpha f^\alpha \rho^\alpha \mathscr{E}^\alpha = \rho \mathscr{E}$. To derive these evolution equations, we begin by expanding the continuity equation (5.10),

$$\frac{\partial f^\alpha}{\partial t} + \frac{\partial(f^\alpha u)}{\partial x} = -\frac{f^\alpha}{\rho^\alpha}\frac{\partial \rho^\alpha}{\partial t} - \frac{f^\alpha u}{\rho^\alpha}\frac{\partial \rho^\alpha}{\partial x}. \tag{5.14}$$

Next, we assume that isotropic stress is maintained during the advection process. Moreover, we assume that any compression that takes place is isentropic and that the entropies of the individual components remain constant. According to these assumptions the pressure change ($\partial \overline{P}$) associated with compression of the bulk will be equal to the pressure change (∂P^α) associated with compression of each component phase,

$$\frac{\overline{K}_S}{\overline{\rho}}\partial\overline{\rho} = \partial\overline{P} = \partial P^\alpha = \frac{K_S^\alpha}{\rho^\alpha}\partial\rho^\alpha. \tag{5.15}$$

Substituting this result we may rewrite (5.14) to give

$$\frac{\partial f^\alpha}{\partial t} + \frac{\partial(f^\alpha u)}{\partial x} = -\frac{f^\alpha \overline{K}_S}{\overline{\rho} K_S^\alpha}\frac{\partial\overline{\rho}}{\partial t} - \frac{f^\alpha \overline{K}_S u}{\overline{\rho} K_S^\alpha}\frac{\partial\overline{\rho}}{\partial x}. \tag{5.16}$$

Finally, (5.16) may be simplified by substitution of the equation of continuity of the bulk, which may be obtained by summing (5.10) over α,

$$\frac{\partial\overline{\rho}}{\partial t} + \frac{\partial(\overline{\rho} u)}{\partial x} = 0, \tag{5.17}$$

to give the thermodynamically self-consistent advection equation for volume fractions:

$$\frac{\partial f^\alpha}{\partial t} + \frac{\partial(f^\alpha u)}{\partial x} = \frac{f^\alpha \overline{K}_S}{K_S^\alpha}\frac{\partial u}{\partial x}. \tag{5.18}$$

The right-hand side of (5.18) is the self-consistent volume fraction change required to maintain isotropic stress while obeying the constraint $\Sigma_\alpha f^\alpha = 1$. Summation of (5.18) gives $\Sigma_\alpha \partial f^\alpha/\partial t = 0$ as required. The volume fractions of the compressible phases (small K_S^α) change most in response to the total divergence.

An internally consistent internal energy equation may be written by adding a $-PdV$ work term to the conservative advection equation. The volume change dV used is that implied by the right-hand side of (5.18):

$$\frac{\partial(f^\alpha \rho^\alpha \mathscr{E}^\alpha)}{\partial t} + \frac{\partial(f^\alpha \rho^\alpha \mathscr{E}^\alpha u)}{\partial x} + \frac{f^\alpha \rho^\alpha}{\overline{\rho}} u \frac{\partial P}{\partial x} = -P\frac{f^\alpha \overline{K}_S}{K_S^\alpha}\frac{\partial u}{\partial x}. \tag{5.19}$$

Since $\Sigma_\alpha \partial f^\alpha = 0$, the summation of (5.19) over α gives the conservative advection equation for total energy, as required.

5.4. *Discretization of Multiphase Equations*

We now present a discretization of (5.10)–(5.12) and (5.18)–(5.19). The volume fraction of phase α in cell i, following advection but prior to any readjustment (i.e., with the right-hand side of (5.18) neglected), is given by a discretization of (5.18),

$$f_i^{\alpha\prime} = f_i^\alpha + \frac{V_{i-1/2}^{\alpha,\text{advected}} - V_{i+1/2}^{\alpha,\text{advected}}}{V_i^{\text{cell}}}, \tag{5.20}$$

where V_i^{cell} denotes the volume of the ith cell. To effect the volume fraction adjustment corresponding to the right-hand side of (5.18) we must next compute an average bulk modulus $\hat{K}_{Si}^\alpha$ for each phase. This is a volume-weighted average that takes account of the cell of origin of the advected fluids and is defined by

$$\frac{f_i^{\alpha\prime}V_i^{\text{cell}}}{\tilde{K}_{Si}^{\alpha}} \equiv \begin{cases} \dfrac{f_i^{\alpha}V_i^{\text{cell}}}{K_{Si}^{\alpha}} + \dfrac{V_{i-1/2}^{\alpha\,\text{advected}}}{K_{S,i-1}^{\alpha}} + \dfrac{V_{i+1/2}^{\alpha\,\text{advected}}}{K_{S,i+1}^{\alpha}}, \\ \qquad \text{if } U_{i-1/2}^{*} > 0 \text{ and } U_{i+1/2}^{*} < 0; \\ \dfrac{f_i^{\alpha}V_i^{\text{cell}} + V_{i-1/2}^{\alpha\,\text{advected}}}{K_{Si}^{\alpha}} + \dfrac{V_{i+1/2}^{\alpha\,\text{advected}}}{K_{S,i+1}^{\alpha}}, \\ \qquad \text{if } U_{i-1/2}^{*} \le 0 \text{ and } U_{i+1/2}^{*} < 0; \\ \dfrac{f_i^{\alpha}V_i^{\text{cell}} - V_{i+1/2}^{\alpha\,\text{advected}}}{K_{Si}^{\alpha}} + \dfrac{V_{i-1/2}^{\alpha\,\text{advected}}}{K_{S,i-1}^{\alpha}}, \\ \qquad \text{if } U_{i-1/2}^{*} > 0 \text{ and } U_{i+1/2}^{*} \ge 0; \\ \dfrac{f_i^{\alpha}V_i^{\text{cell}} + V_{i-1/2}^{\alpha\,\text{advected}} - V_{i+1/2}^{\alpha\,\text{advected}}}{K_{Si}^{\alpha}}, \\ \qquad \text{if } U_{i-1/2}^{*} \le 0 \text{ and } U_{i+1/2}^{*} \ge 0. \end{cases} \tag{5.21}$$

The adjusted volume fractions are

$$f_i^{\alpha,n+1} = f_i^{\alpha\prime} + \left(1 - \sum_{\beta} f_i^{\beta\prime}\right)\frac{f_i^{\alpha\prime}\hat{K}_{Si}}{\tilde{K}_S^{\alpha}} \tag{5.22}$$

where the phase average bulk modulus $\hat{K}_S$ is computed from the single-phase quantities $\tilde{K}_S^{\alpha}$ using (5.6).

The advected fluxes in a single-phase Godunov method are computed from the solution to the Riemann problem. Here, in our multiphase method where the Riemann problem is solved for an effective single phase, we have a valid estimate of u^*, v^*, and P^*, but not of the single-phase quantities $\rho^{\alpha *}$ and $\mathscr{E}^{\alpha *}$. In their place we use the appropriate upwind quantities:

$$\begin{pmatrix} \tilde{\rho}_{i+1/2}^{\alpha *} \\ \tilde{\mathscr{E}}_{i+1/2}^{\alpha *} \end{pmatrix} = \begin{cases} \begin{pmatrix} \rho_i^{\alpha} \\ E_i^{\alpha} + \frac{1}{2}(u^{*2} + v^{*2}) \end{pmatrix} & \text{if } u^* > 0; \\ \begin{pmatrix} \rho_{i+1}^{\alpha} \\ E_{i+1}^{\alpha} + \frac{1}{2}(u^{*2} + v^{*2}) \end{pmatrix} & \text{if } u^* \le 0. \end{cases} \tag{5.23}$$

We have validated the approximation given in (5.23) by comparing computations obtained with this approximation to computations obtained with an "exact" multiphase Riemann solver in which the individual phase properties are directly available. Our comparisons indicate that the overall solution is insensitive to this approximation. A detailed description of the "exact" multiphase Riemann solver we used is presented in the Appendix.

With these approximate quantities, the mass, momentum, and energy updates are

$$f_i^{\alpha,n+1}\rho_i^{\alpha,n+1} = f_i^{\alpha}\rho_i^{\alpha} + \frac{V_{i-1/2}^{\alpha\,\text{advected}}}{V_i^{\text{cell}}}\tilde{\rho}_{i-1/2}^{\alpha *} - \frac{V_{i+1/2}^{\alpha\,\text{advected}}}{V_i^{\text{cell}}}\tilde{\rho}_{i+1/2}^{\alpha *} \tag{5.24}$$

$$\rho_i^{n+1}u_i^{n+1} = \rho_i u_i + \frac{\Delta t}{\Delta x}\left[(\tilde{\rho}_{i-1/2}^{*}u_{i-1/2}^{*2} + P_{i-1/2}^{*}) - (\tilde{\rho}_{i+1/2}^{*}u_{i+1/2}^{*2} + P_{i+1/2}^{*})\right] \tag{5.25}$$

$$\rho_i^{n+1}v_i^{n+1} = \rho_i v_i + \frac{\Delta t}{\Delta x}\left[(\tilde{\rho}_{i-1/2}^{*}u_{i-1/2}^{*}v_{i-1/2}^{*}) - (\tilde{\rho}_{i+1/2}^{*}u_{i+1/2}^{*}v_{i+1/2}^{*})\right] \tag{5.26}$$

$$\begin{aligned} f_i^{\alpha,n+1}\rho_i^{\alpha,n+1}\mathscr{E}_i^{\alpha,n+1} = {} & f_i^{\alpha}\rho_i^{\alpha}\mathscr{E}_i^{\alpha} + \frac{V_{i-1/2}^{\alpha\,\text{advected}}}{V_i^{\text{cell}}}\tilde{\rho}_{i-1/2}^{\alpha *}\tilde{\mathscr{E}}_{i-1/2}^{\alpha *} \\ & - \frac{V_{i+1/2}^{\alpha\,\text{advected}}}{V_i^{\text{cell}}}\tilde{\rho}_{i+1/2}^{\alpha *}\tilde{\mathscr{E}}_{i+1/2}^{\alpha *} \\ & + \frac{\Delta t}{\Delta x}\frac{f_i^{\alpha,n+1}\rho_i^{\alpha,n+1}}{\overline{\rho}_i^{n+1}}(P_{i-1/2}^{*} - P_{i+1/2}^{*}) \\ & - P\left(1 - \sum_{\beta} f_i^{\beta\prime}\right)\frac{f_i^{\alpha\prime}\overline{K}_{Si}}{\tilde{K}_S^{\alpha}}, \end{aligned} \tag{5.27}$$

where

$$\tilde{\rho}_{i-1/2}^{*} = \frac{\sum_{\alpha} V_{i+1/2}^{\alpha\,\text{advected}}\tilde{\rho}_{i-1/2}^{\alpha *}}{\sum_{\beta} V_{i+1/2}^{\beta\,\text{advected}}}. \tag{5.28}$$

5.5. *Pressure Relaxation*

Following the multiphase conservative updated described in (5.24)–(5.27) above, the multiple phases in any single cell may not be in mechanical equilibrium ($P^{\alpha} \neq P^{\beta}$). A procedure for reaching mechanical equilibrium is described here. We seek a new pressure, common to all phases, $\overline{P}$, such that mechanical equilibrium will be achieved while the constraint $\Sigma_{\alpha} f^{\alpha} = 1$ is observed. This may be accomplished by solving the following set of equations for the changes in volume fraction f^{α}:

$$\overline{P} = P^{\alpha} + \Delta P^{\alpha} = P^{\alpha} - \frac{K_S^{\alpha}}{f^{\alpha}}\Delta f^{\alpha} \tag{5.29}$$

$$\sum_{\alpha} \Delta f^{\alpha} = 0. \tag{5.30}$$

The resulting volume fraction update is

$$\overline{P} = \sum_{\alpha} \frac{f^{\alpha}P^{\alpha}}{K_S^{\alpha}} \Big/ \sum_{\alpha} \frac{f^{\alpha}}{K_S^{\alpha}} \tag{5.31}$$

$$\Delta f^{\alpha} = \frac{f^{\alpha}}{K_S^{\alpha}}(P^{\alpha} - \overline{P}) \tag{5.32}$$

$$f^\alpha \leftarrow f^\alpha + \Delta f^\alpha. \tag{5.33}$$

Conservation of mass dictates a density update

$$\rho^\alpha \leftarrow \frac{f^\alpha \rho^\alpha}{f^\alpha + \Delta f^\alpha}, \tag{5.34}$$

and the self-consistent isentropic $-PdV$ internal energy update is

$$f^\alpha \rho^\alpha E^\alpha \leftarrow f^\alpha \rho^\alpha E^\alpha - \overline{P}\Delta f^\alpha. \tag{5.35}$$

These equations are implemented, possibly iteratively, in conjunction with equation of state evaluations that determine the pressures P^α and isentropic bulk moduli K_S^α of each phase.

In some experiments we have found that the relative volume change $\Delta f^\alpha / f^\alpha$ called for in the pressure equilibration step is too large to be compatible with the linearization implicit in (5.29). In some cases this leads to extrapolation into regions of thermodynamic space where the equation of state model we used was unstable. To prevent this pathological behavior the procedure outlined above is modified by enforcing a limit on the maximum allowed change in $\Delta f/f$. We define two constants: δ_- is the largest $|\Delta f/f|$ allowed for compression, and δ_+ is the largest value allowed for expansion. We used the numerical values $\delta_- = 0.1$ and $\delta_+ = 0.05$. The limited fraction change in a binary system is then given by

$$\Delta f^1 \leftarrow \begin{cases} \min(\Delta f^1, \delta_+ f^1, \delta_- f^2, 1 - f^1) & \text{if } \Delta f^1 > 0; \\ \max(\Delta f^1, -\delta_- f^1, -\delta_+ f^2, f^2 - 1) & \text{otherwise.} \end{cases} \tag{5.36}$$

It is in this pressure relaxation step of our multiphase algorithm that we implement spallation. If the pressure within a vacuum-free (possibly single phase) cell is negative and larger in magnitude than the yield strength (which we currently treat as a constant adjustable parameter) then vacuum is introduced and the condensed phases are relaxed to zero pressure with the procedure outlined above. As indicated in Fig. 4e, spallation ought to be a feature of the Riemann solver. Our choice was based on a desire to separate all multiphase considerations from the effective single-phase integrator, which includes the Riemann solver.

5.6. *Summary of the 1D Multiple-Phase High-Order Godunov Method*

In detail, the multiphase algorithm consists of the following steps:

(i) Evaluate the equation of state for each phase in each cell to determine the quantities P, K_S, and K_S'.

(ii) Construct an effective single phase by averaging density $\overline{\rho}$ (5.2), internal energy $\overline{E}$ (5.3), isentropic bulk modulus $\overline{K}_S$ (5.6), and the isentropic pressure derivative of $\overline{K}_S$, $\overline{K}_S'$ (5.7).

(iii) Construct the flattening parameter χ (4.17)–(4.19). In multiphase applications we set the parameter $\overline{\chi}$ (4.18) to zero in multiphase cells.

(iv) Compute limited slopes for the quantities $\overline{\rho}$, u, v, P, and $\overline{E}$ (4.15)–(4.20).

(v) Use upwind characteristic tracing to construct L and R states centered at the half time step at each cell edge (4.11)–(4.14).

(vi) Solve the Riemann problem at each edge. Compute the pressure P^*, the velocities u^* and v^*, and the internal energy E^* of the state that lies on the zero-velocity characteristic.

(vii) Compute the conserved fluxes (4.3), and update the conserved quantities for those cells that contain only a single phase (4.7). The fluxes at single-phase edges include an artificial viscosity term (4.21)–(4.23).

(viii) For each multiphase edge, implement a second-order volume-of-fluid interface reconstruction routine to determine the signed volumes $V_{i+1/2}^{\alpha\,\text{advected}}$ of each phase advected across the edge with velocity u^*.

(ix) Update the volume fractions (5.20)–(5.22), densities (5.24), momenta (5.25), (5.26), and energies (5.27).

(x) Relax multiphase cells to mechanical equilibrium. For each phase in each multiphase cell evaluate the equation of state to determine the pressure P^α and isentropic bulk modulus K_S^α. Adjust volume fractions (5.31)–(5.33), densities (5.34), and internal energies (5.35). This step may be iterated depending on the problem and the accuracy required.

5.7. *One-Dimensional Test Problems*

We now present the results of three one-dimensional test problems designed to highlight various features of our method.

A ''smooth'' rarefaction fan. First we present the results from a computation of the inside of a centered rarefaction in aluminum (Al). This is an example of ''smooth flow'' where we expect second-order convergence of our method. The material properties of Al we used are those reported in Marsh [28] and shown in Table I. We computed the ''exact'' rarefaction solution in aluminum by using a fourth-order Runge–Kutta method to integrate the ODEs

$$\frac{du}{dp} = (\rho c)^{-1} \tag{5.37}$$

TABLE I

Equation of State Parameters

Property	Value	Dimensions
Aluminum[a]		
ρ_0	2.785	Mg/m^3
c_0	5.328	km/s
s	1.338	
γ_0	2.0	
q	1	
P_0	0	GPa
T_0	298	K
MORB[b]		
$\rho 0$	2.66	Mg/m^3
c_0	2.10	km/s
s	1.68	
γ_0	0.18	
q	1	
P_0	0	GPa
T_0	1673	K
C_V^c	0.0012	MJ/kg · K
Molybdenum[d]		
ρ_0	9.961	Mg/m^3
c_0	4.77	km/s
s	1.43	
γ_0	1.56	
q	1	
P_0	0	GPa
T_0	1673	K
C_V^b	0.00026	MJ/kg · K

[a] Ref. [28].
[b] Ref. [41, 40]
[c] C_V is based on 3k/atom approximation.
[d] Ref. [34].

$$\frac{d\rho}{dp} = \rho/K_s \tag{5.38}$$

starting from the right state $V_R = 1/\rho_0$, $P = 0$, $u = u_R$ until we reached the left state $V_L = 0.3416$, $P = 4.390$, $u = u(V_R)$. The velocity $u_R = -6.0457$ was chosen so that the $u - c$ characteristic state halfway through the fan (at $V = (V_R + V_L)/2$) was stationary. The quantities (ρ, E, u, and $u - c$) at each step of the numerical integration were tabulated.

The initial conditions were generated by picking a starting time $t_0 = 1$ μs and associating each coordinate x in the problem domain $[-0.5$ mm, 0.5 mm) with a characteristic; $x/t_0 = u - c$. The values of (ρ, E, and u) corresponding to the characteristic $u - c$ were obtained by interpolation of the tabulated results. Boundary data at each time step of the computation was derived similarly by interpolating with the appropriate characteristic $x/t = u - c$.

We compared the computed solution with the "exact" one at time $t = 2.5$ μs. We computed the L_1, L_2, and max norms of the error in the density, momentum, and total energy at this time. The results are shown in Table II. This test problem yielded a convergence rate of between 1.9 and 2.6—depending on the quantity and the norm—verifying that our method achieves second-order accuracy in regions of smooth flow. The initial and final profiles are shown in Fig. 9.

Wilkins' test problem. Next we present a 1D test problem from Wilkins [48] in which a 4-mm piece of aluminum, traveling at 2 km/s, impacts an aluminum half space (Fig. 10). In our computation of this problem we used a problem domain 25 mm wide, from say 0 to 25, in which the 4-mm projectile initially occupies coordinates 1–5, the Al half-space occupies coordinates 6–25, and the rest of the domain is vacuum. The computation shown in Figs. 10a–10f was done on a 500-cell domain with CFL 0.3 and artificial viscosity parameter $\zeta = 0.02$. Figure 10g shows the L_1 density errors at time 5 μs derived by comparing the computation shown above with similar computations on 250-cell and 125-cell domains. Peaks in the error spectrum occur at the free surface, the projectile–target interface (a double peak, exaggerated by "startup errors" [16]), both ends of the rarefaction fan (first order in smoothness), and the shock (zero order smoothness). Figure 10h is the order of accuracy derived from Fig. 10g. The average order of accuracy shown here is 1.75.

A test problem that includes spallation. This computation (Fig. 11) demonstrates how our method currently handles spall. Shown is a 30-mm-thick bar of aluminum in a vacuum. Initially the Al has zero velocity and pressure, density, and internal energy given by $(P, \rho, E) = (3.277, 21.841, 0.588)$. (This corresponds to a state on the principal Hugoniot for which $U_P = 1.0$.) Left and right rarefactions pass through the material, creating tension when they collide. Vacuum is introduced when the pressure drops below -2.0 GPa. The abrupt change from -2.0 GPa to 0 caused by the spallation process drives large amplitude acoustic

TABLE II

The Error and Convergence Rate in Computing the Interior of a Rarefaction Fan in Aluminum

Cells	1-Norm	Rate	2-Norm	Rate	Max norm	Rate
Density						
16	1.4322D-06		3.6511D-07		1.9057D-06	
32	3.6165D-07	2.0	6.4392D-08	2.5	4.6810D-07	2.0
Momentum						
16	1.7623D-07		5.1802D-08		4.2595D-07	
32	4.2375D-08	2.0	8.7082D-09	2.6	1.1160D-07	1.9
Energy						
16	2.2395D-05		5.7097D-06		2.9053D-05	
32	5.6538D-06	1.9	1.0080D-06	2.5	7.1863D-06	2.0

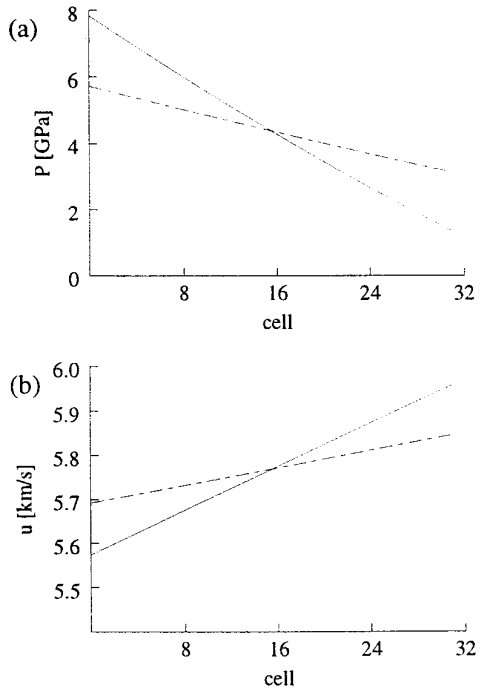

FIG. 9. A rarefaction fan in aluminum centered on the grid: (a) pressure before (solid) and after (dashed) 1117 iterations on a 32-cell grid with CFL 0.5; (b) velocity before (solid) and after (dashed) 1117 iterations. Initial and boundary conditions are supplied by "exact" calculation. This computation was repeated with 16 cells, requiring 560 iterations to reach the same time. A comparison of the L_1 norm density errors, based on comparison to exact results, reveals second-order convergence.

waves that are evident in both the pressure and velocity profiles. This spallation procedure initially creates a large number of cells that contain a mixture of aluminum and vacuum: a distinct material interface is not initially present. With time the material coalesces, and distinct regions of material separated by distinct regions of vacuum emerge. This computation was done on a 400-cell domain with CFL 0.8.

6. ADAPTIVE MESH REFINEMENT

To model two-dimensional problems, the one-dimensional multiphase method for integrating Eqs. (4.1) presented above is driven by an adaptive mesh refinement (AMR) application shell that (1) breaks the physical domain into a number of two-dimensional rectangular grids, (2) manages the integration of (4.1) on these grids such that the grid–grid and grid–domain edge boundary conditions are consistently maintained in time, and (3) dynamically maintains a hierarchy of higher-resolution subgrids whose placement may be controlled to reduce local errors and provide enhanced spatial resolution. The AMR strategy in the context of a system of hyperbolic conservation laws is described in [7–10], and our independently coded C++/FORTRAN hybrid implementation is based on the algorithms defined in these references. Here, we describe details of this algorithm that are specific to our multiphase integrator and its application described in the following section.

There are several processes in the AMR algorithm that require special consideration in multiphase computations. Foremost among these is the creation of fine grid patches. When a coarse grid patch is projected onto a refined grid patch, simple polynomial interpolation of the cell-centered quantities $\mathscr{U}$ may lead to a smearing of phase boundary interfaces across several fine grid cells. In the application described in the following section we store the following eight cell-centered quantities:

$$\mathscr{U} = \begin{pmatrix} \overline{\rho} = f_1\rho_1 + f_2\rho_2 \\ \overline{\rho}u \\ \overline{\rho}v \\ \overline{\rho}\overline{\mathscr{E}} = f_1\rho_1\mathscr{E}_1 + f_2\rho_2\mathscr{E}_2 \\ f_1 \\ f_1\rho_1 \\ f_1\rho_1\mathscr{E}_1 \\ f_v \end{pmatrix}. \tag{6.1}$$

Here f_1 is the volume fraction of phase 1 and f_v is the volume fraction of vacuum in a cell. Neither of these is a conserved quantity. Moreover, the phase volume fractions are not smoothly varying functions within a cell. They assume values of 0 or 1 in single-phase regions and take fractional values only in regions of space that straddle the interphase boundary.

There are two approaches to rectifying this problem. First, when a grid patch containing a phase boundary is projected onto a refined grid, an interface reconstruction routine, such as that described in Section 5.2, may be used. Only those fine grid cells that straddle the reconstructed interface will then contain more than one phase and interface smearing will not occur. An alternative approach is to require that multiphase cells always be refined at the maximum resolution. When this is done the fine multiphase grids are filled by the initialization subroutines instead of by interpolation from coarse grid cells. Since the interfaces are always computed with the maximum level of refinement, the interpolation of multiphase coarse cells is never necessary. Since the computational cost of refined grid patches greatly exceeds that of coarser grids, this strategy is computationally expensive. Nevertheless, we adopt this second strategy in the computations shown here, since in these computations we are principally concerned with resolving features associated with the interfaces.

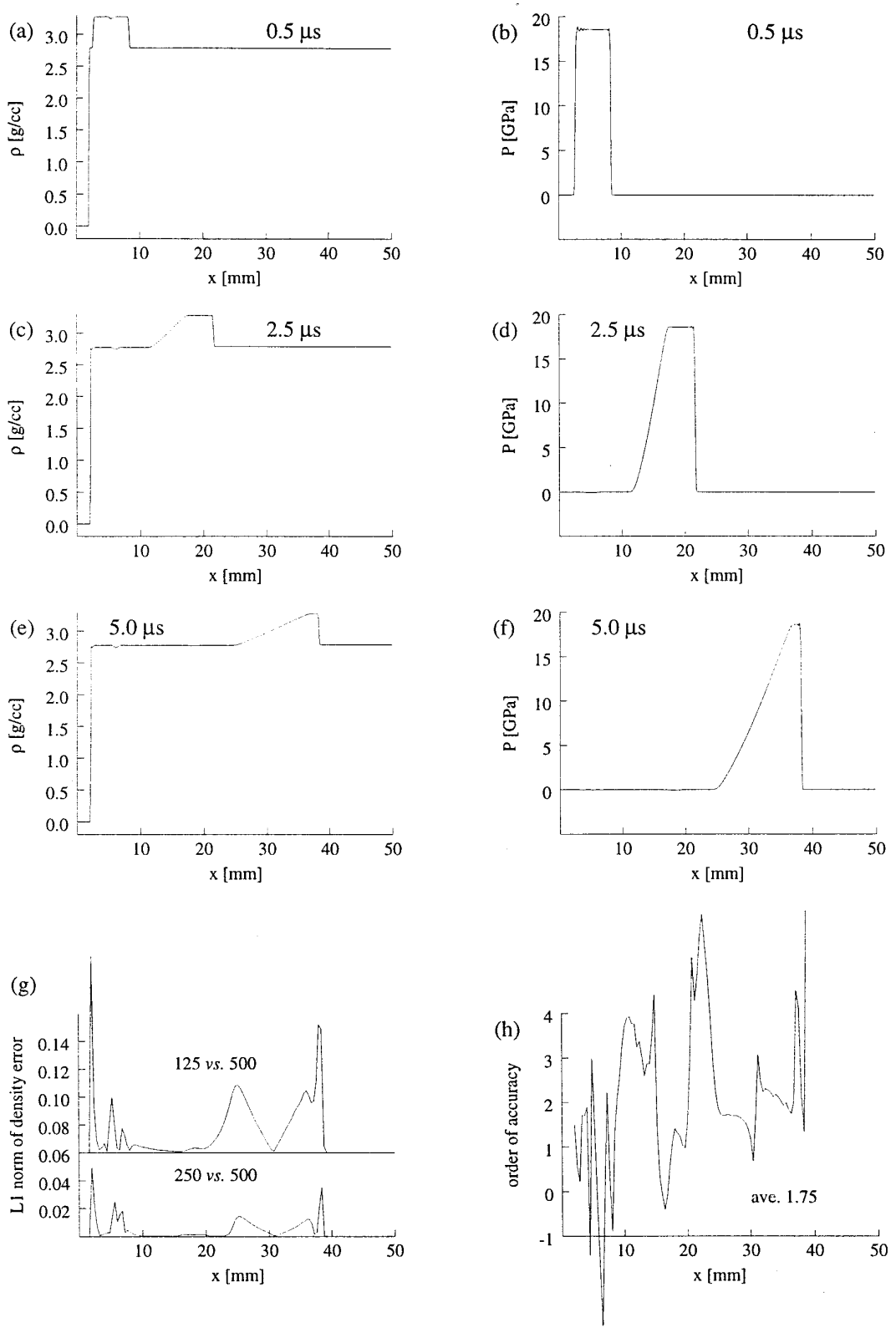

FIG. 10. Wilkins' problem: (a) density and (b) pressure at 0.5 μs; (c, d) same at 2.5 μs; (e, f) and 5.0 μs. (g) L_1 denstiy errors comparing 500-, 250-, and 125-cell calculations at 5.0 μs; and (h) order of convergence.

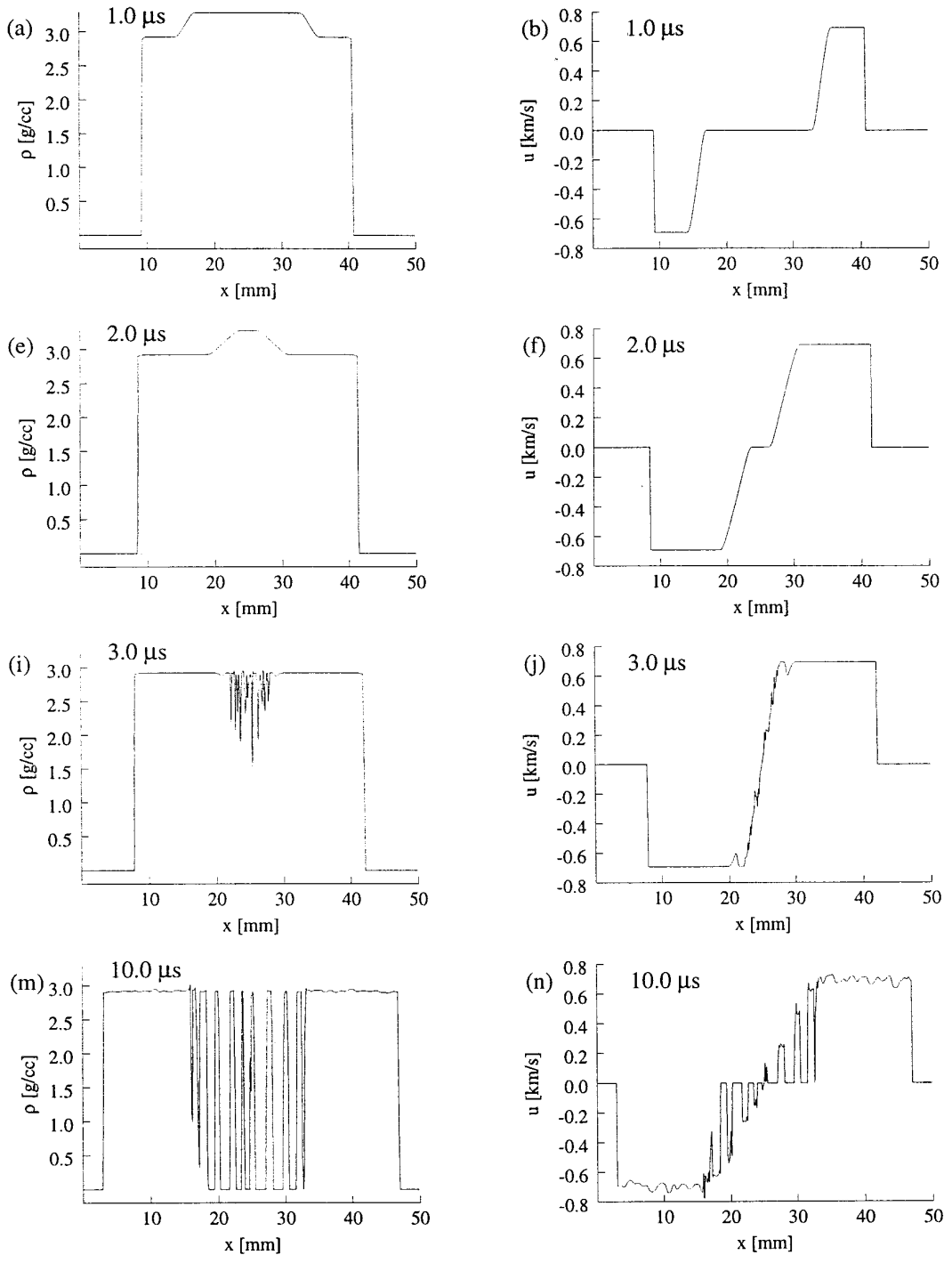

FIG. 11. Release of a compressed aluminum bar leading to spall: (a) density, (b) velocity, (c) pressure, and (e) vacuum volume fraction at 1.0 μs. (e–h) Same at 2.0 μs, (i–l) at 3.0 μs, and (m–p) at 10.0 μs.

There are other processes in the AMR algorithm that are robust when each cell-centered quantity is a conservative density, but are somewhat problematic when there are cell-centered quantities such as phase volume fractions that are not conservative. One algorithm within AMR that leads to discrepancies with our nonconserved cell-centered quantities is the matching of coarse grid and neighboring fine grid cell boundary fluxes. To simultaneously manage nested fine

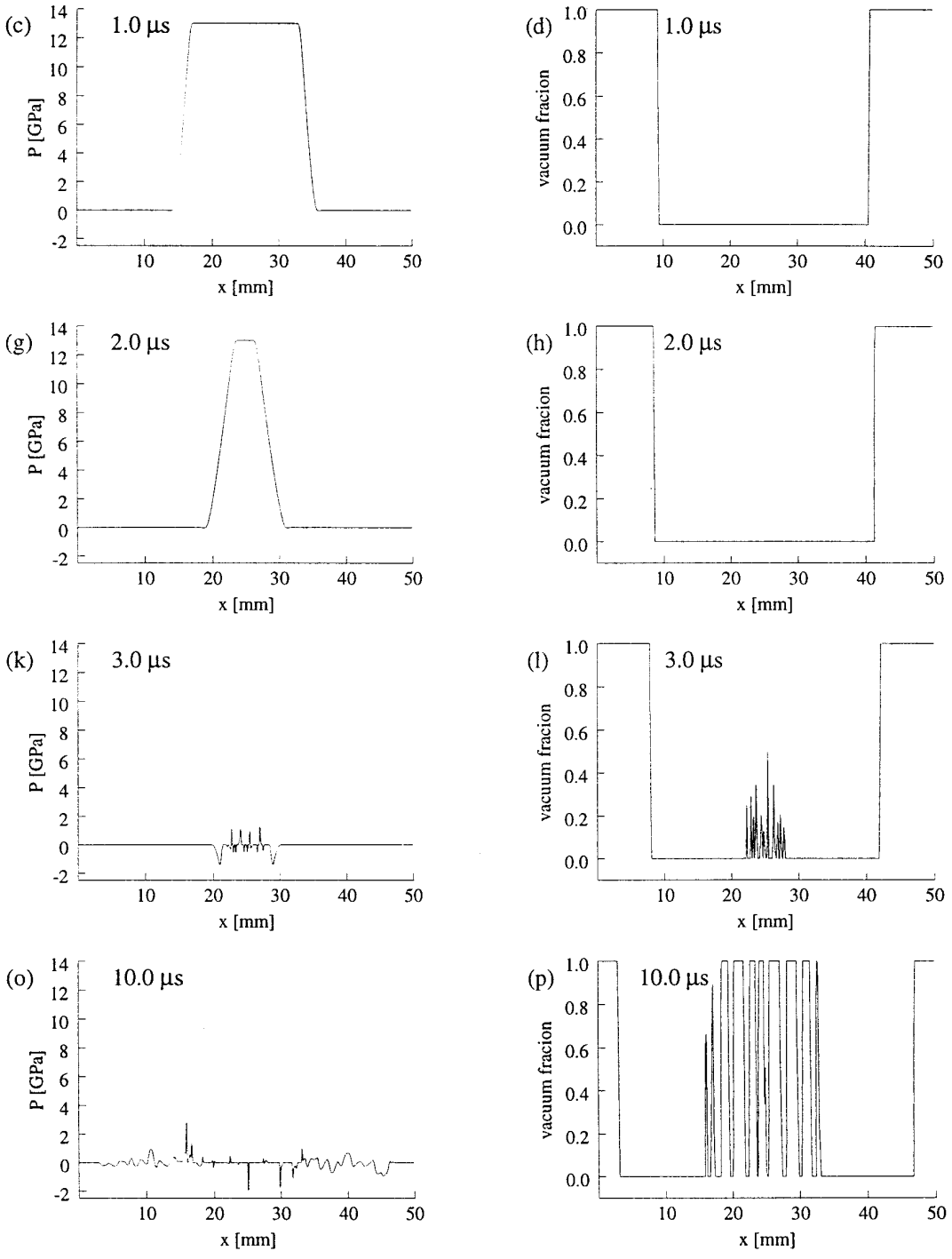

FIG. 11—*Continued*

and coarse grid hierarchies conservatively requires that the fine-grid boundary fluxes and the neighboring coarse-grid cell boundary fluxes be made equal over each coarse time step. For example, suppose that within a particular coarse grid there is a fine subgrid with four times greater spatial resolution. The fine subgrid will be integrated four times with time step $\Delta t_{\text{fine}} = \Delta t_{\text{coarse}}/4$ for each integration of the surrounding coarse grid. At the end of that coarse time step the coarse cell edge flux computed on the coarse grid must equal the sums over four fine time steps of the four neighboring fine cell edge fluxes. To accomplish this the coarse cell edge flux is adjusted to equal the computed

total flux from the fine cell edges. When this adjustment is done on nonconserved variables, such as phase volume fractions, the adjusted coarse cell quantities $\mathscr{U}$ will become incompatible to some degree. Specifically, the condition of mechanical equilibrium (i.e., equality of stresses) will be violated and hence a pressure equilibration, as discussed in Section 5.5, is required.

To remedy this problem we could implement the pressure equilibration algorithm during the flux readjustment AMR step. However, this is not necessary when the material interfaces are always resolved on the finest grid patches. Since the interface is interior to the fine grid patches, the interface fluxes between fine and neighboring coarse grid cells are always single phase.

Refined grids are created to reduce local truncation error, which is estimated using a method based on Richardson extrapolation [9]. Specifically, the local error τ is estimated by

$$\frac{\mathscr{I}_h^2 \mathscr{U} - \mathscr{I}_{2h} \mathscr{U}}{2^{p+1} - 2} = \tau + O(h^{p+2}), \tag{6.2}$$

where $\mathscr{I}_h^2$ denotes the two-level finite difference operator, applied twice with time step Δt_h, and $\mathscr{I}_{2h}$ is the same operator but applied once with time step $\Delta t_{2h} = 2\Delta t_h$ to a grid coarsened by a factor of 2 in each direction. Here, p is the order of accuracy in space and time of the operator $\mathscr{I}_h$, which we take to be 2, and h is the length of a cell on the original grid. This estimate is performed every two time steps (this is an adjustable parameter) and compared to a user-defined error tolerance threshold. When that tolerance is exceeded the offending region is tagged for additional refinement.

In the work that follows, we compare the error in average density $\bar{\rho}$ using a threshold $\tau_{\max} = 10^{-4} \mathscr{I}_{2h} \mathscr{U}$. We set the truncation error τ to some large number at each phase boundary. This ensures that the phase boundaries will lie within the most refined cells and thereby avoid the problems described above. We also employ refinement criteria other than (6.2). For the application discussed below we want to resolve the shock front and steep rarefaction fans with the highest resolution. To accomplish this we also evaluate the divergence of the velocity field and assign some large (fictitious) truncation error to those cells with a large absolute values ($|\nabla \cdot u| > 2/\mu$s).

7. AN APPLICATION TO EXPERIMENTAL SHOCK WAVE STUDIES

7.1. *A Computational Study*

We have used the method described above to study the propagation of edge effects in multiphase assemblies used in geophysical shock wave laboratory experiments [35].

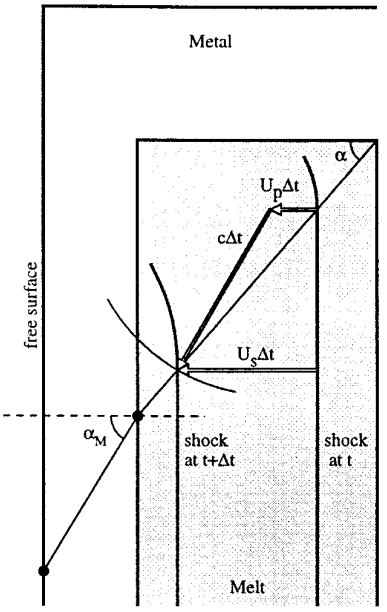

FIG. 12. Sound speed determination from edge effects after [6]. In time Δt the edge disturbance (originating at a corner, for instance) is advected a distance $U_P \Delta t$ with particle velocity U_P and at the same time radiates a distance $c\Delta t$ at the sound speed c in all directions. The intersection of this surface with the shock (which travels a distance $U_S \Delta t$) defines a ray of angle α, where $U_S^2 \tan^2\alpha = c^2 - (U_S - U_P)^2$. When the shock reaches the melt-metal interface the edge effect will propagate at the different angle α_M. This angle is computed as indicated above, but with the velocities relevant for the shocked metal.

This was done to assess whether the compressional edge effects in the experiments described in [36] propagate as acoustic waves—at the sound speed of the shock-compressed sample [6]—or as oblique shocks. We determined that the edge effects were acoustic and that the experiments were therefore analyzed in an internally consistent way. Preliminary work extending our earlier study is presented here.

Al'tshuler *et al.* [6], in experiments known to have acoustic edge effects, tried to measure the angle of intersection of the moving shock wave with the acoustic edge effect signal for the purpose of obtaining sound speeds under shock-loading conditions. They detected the shock arrival on the free surface of their samples and looked for the onset of curvature to indicate the interference of edge effects with the otherwise planar shock. Experiments with encapsulated melts (Fig. 12) are complicated by the propagation of the edge signal through the container, but have qualitatively similar features. In principle, the sound speed of an encapsulated liquid may be measured by observing edge effects on the container surface.

Here we consider two questions relevant to the propagation of edge effects in encapsulated melts (Fig. 12). First, "Given probable experimental errors in the detection of

free surface motion, is it possible to detect the initial interaction of the edge effects with the otherwise planar shock at the free surface of the container?'' It is not obvious that this should be the case because the strength of the leading edge of the acoustic disturbance is weak and might be undetectable after propagation through the metal container. The experimentally detectable onset of edge effects might be unacceptably different from the idealized model shown in Fig. 12, or if the onset of shock front distortion is compatible with the idealized model, the angle α in the melt, and hence the melt sound speed might be deduced. In actual practice the inference of α in a single experiment will be contingent on determination of the angle α_M that describes the propagation of edge effects in the metal container. The angle α_M may be computed for some materials, but will depend on whether a plastic shock or an elastic precursor is the wave detected by the experimental apparatus. Alternatively, two experiments with identical container thickness but different melt thickness could be used to experimentally account for α_M, regardless of whether the leading disturbance detected at the free surface is elastic or plastic.[2] In this study we will assume the molybdenum container has zero material strength. Although this is inconsistent with experiment [18], it is an adequate assumption for the purpose of assessing the feasibility of melt sound speed measurement.

The region of the liquid sample influenced by edge effects is dispersive and covers a range of pressures, which is about 10 GPa in the experiments described below. The leading edge of the affected region is determined by the sound speed of the sample under the shock conditions that pertain where the shock is planar. However, within the large affected region the distribution of thermodynamic and hydrodynamic properties will be sensitive to the sample's pressure-dependent sound speed over the range of pressures found in the affected region. In the context of the thermodynamic model discussed in Section 2 above, the details of the region affected by edge signals will depend on both γ_0 and q (see (2.16)). Thus the second question we address in this section is, ''Is the detected free surface arrival sufficiently sensitive to the parameters γ_0 and q that an inverse method might be constructed to deduce these parameters from the measured free surface record across the width of the region influenced by edge effects?'' The first question addresses the detectability of the onset of edge effects at the free surface; the second question examines the information content of the record within the affected region.

These investigations are motivated by the experiments illustrated in Fig. 13, which are currently being conducted by the first author for the purpose of determining the Hugoniot EOS of silicate liquids. If the experimental data, particularly the streak camera record, contain information on the sound speed and also possibly on the volume dependence of the sound speed, then that information is available at no additional experimental cost. A separate issue, not taken up, is, ''How might the target be redesigned to optimize the sensitivity of the streak record to the sound speed information?'' To address that question, parameters that we consider here to be invariant, such as the metal plate thicknesses and metal–liquid interface angles, could be changed.

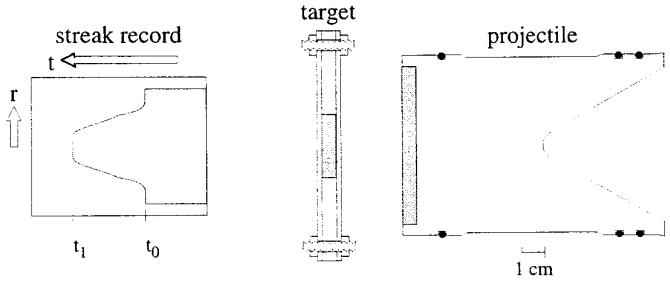

FIG. 13. Experimental setup. A projectile, consisting of a polycarbonate sabot carrying a 6.4-mm-thick metal plate, is accelerated to between 1.0 and 2.5 km/s by an 80-mm-diameter single-stage gun. The projectile strikes a target assembly made of molybdenum plates and containing a silicate glass. Prior to impact the target assembly is induction-heated to above the liquidus of the silicate composition. The (left) free surface of the target is observed with a streak camera. The streak camera records the light reflected off the free surface in one spatial (r) and as a function of time (t). The reflectivity changes when the shock reaches the free surface. Shown is t_0, the time when a planar shock reached the free surface after traversing three layers of molybdenum, and t_1, the time when a planar shock traversed a layer of molybdenum, the liquid sample, and a second layer of molybdenum. The relative time ($t_1 - t_0$) determines a point on the liquid Hugoniot [36].

We present the results of three computations (Table III) which we have conducted to address the first two questions. In the first computation, we model the propagation of a planar shock through a molybdenum container and into an encapsulated liquid sample (midocean ridge basalt, MORB) using the experimentally determined thermodynamic parameters shown in Table I. The simulated system is 10×10 mm on an initial 100×100 coarse grid. One level of grid refinement is allowed, with the fine grid cells one-fourth the size of the coarse cells. The system is in cylindrical coordinates with the bottom edge being the axis of symmetry. The computations described below took approximately 50 CPU-min each on a Cray C90.

The sequence of events for the first run is illustrated in Fig. 14: the results shown apply qualitatively to the other runs, too. The first snapshot shown illustrates the starting configuration: a left-traveling planar shock in molybdenum

[2] An edge effect will be seen in the surrounding metal, but the nominal pressure there is different from that in the material to the left of the liquid. The angles α_M in the metal adjacent to the liquid cannot, therefore, be deduced by a measurement of α_M in the surrounding metal.

TABLE III

Run Parameters

Property	Value
All Runs	
P in Mo.	60.8 GPa
P in MORB.	20.2 GPa
Run 1	
γ_0	0.18
q	1
c at 20.2 GPa	5.93 km/s
α	46.3°
α_M	29.3°
Run 2	
γ_0	1.0
q	1
c at 20.2 GPa	5.62 km/s
α	44.2°
α_M	29.2°
Run 3	
γ_0	0.18
q	−3.23
c at 20.2 GPa	5.62 km/s
α	44.2°
α_M	29.0°

is 303 ns away from striking the molybdenum–MORB interface. The initial shock has a strength of 60.8 GPa. When the shock reaches the interface, a weaker 20.2-GPa shock is transmitted to the MORB, and a right-traveling rarefaction is reflected into the molybdenum. Away from the corner, the plane 60.8-GPa molybdenum shock continues unperturbed. The second snapshot shows the configuration 358 ns after the shock reached the molybdenum–MORB interface. Note that the edge effect generated at the corner is compressive inside the MORB, and expansive in the molybdenum. After traversing the encapsulated MORB, the shock reaches the left molybdenum–MORB interface. When that occurs a shock is transmitted into the molybdenum and a right-traveling shock is reflected back into the MORB. The strength of this second shock is about 45.4 GPa. Being a recentered shock in the MORB, this shock is slightly sensitive to the thermodynamic model parameters γ_0 and q, and is therefore different in each of the three computations. The third snapshot, at 628 ns after initial interaction of the shock with the MORB, shows the development of the reflected wave structure. The plane shock in the MORB has not yet reached the second molybdenum–MORB interface, but a reflected shock wave structure has begun to develop where it has been bent forward (to the left) by the edge effects. The final snapshot, at 756 ns after initial impact, shows a right-traveling rarefaction fan that has reflected off of the molybdenum free surface at the top of the simulated system. At the bottom, adjacent to the encapsulated MORB, the left-traveling shock has not yet reached the free surface.

At each fine-grid time step we monitor the velocity of the free surface. We arbitrarily mark the free surface when its velocity reaches 10 m/s; we assume this to be the onset of detectable surface motion that might be recorded on a streak camera. The time-radius history of these first motions constitutes a synthetic streak record (Fig. 13). These measurements are at discrete intervals of approximately 1 ns, which is comparable to instrumental uncertainties. The synthetic streak records for our three simulation runs are shown together in Fig. 15. Note that some offset of these records is evident even where the shock is planar when it reaches the free surface; the magnitude of this error is within one fine-grid time step. It may be explained by the fact that the time steps in each simulation are determined independently by the requirement that the CFL number, $c\Delta t/\Delta x$, not exceed a defined threshold, which is 0.4 in our case. Since the sound speeds c differ in each of the three computations, the time steps Δt differ correspondingly. Thus the time intervals at which the free surface motion is examined are different in each computation.

It is also evident on examination of Fig. 15 that the distance between the radial coordinate of the outer metal–liquid interface and the location of the first detectable edge effects on the free surface are about 10% smaller than their theoretical values. To a first approximation this suggests a systematic bias of 10% of tan α, with corresponding systematic errors that affect the inferred sound speed. This answers in part the first question we posed. The onset of edge effects on the free surface motion are not detectable without bias. Underestimation of the radial extent of the edge signal leads to underestimates of c and overestimation of γ. Therefore experimental results must be interpreted with some caution.

The second and third computations are characterized by equal high-pressure sound speeds that are about 5% lower than those in the first computation. The value of α for both of these runs is identical, but the value of α_M differs somewhat, since the recentered Hugoniots of the modeled liquids differ. The second computation has a greatly increased value of γ_0, whereas the third computation has a greatly reduced value of q. These values are substantially different, and in no way constitute small perturbations from the experimentally determined parameter set that we used in the first computation. Nevertheless, the free surface wave forms of these runs do not differ materially. Their offset in time is within the error of the synthetic streak records and also within experimental uncertainties. Therefore the answer to the second question is negative. The free surface motion is insensitive to the pressure dependence of the liquid sound speed with as

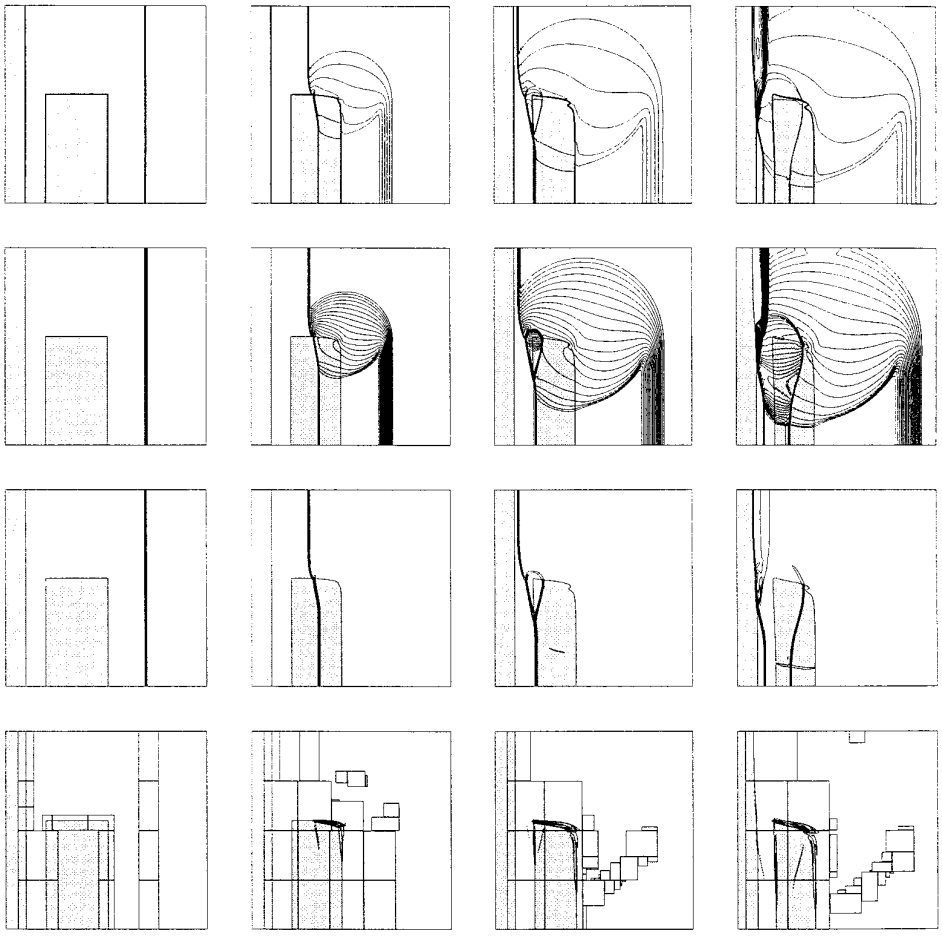

FIG. 14. Simulation of a left-traveling shock in molybdenum interacting first with an encapsulated MORB liquid and then with a free surface. Contour plots of density (first row), pressure (second row), velocity divergence (third row), and vorticity with superimposed AMR fine-grid structure (fourth row). The relative times are −303 ns (first column), 358 ns (second column), 628 ns (third column), and 756ns (fourth column). The vacuum boundary condition at the left side of the problem domain is shaded, as is the approximately rectangular MORB sample region in the interior. The molybdenum container is unshaded.

much as 10 GPa leverage on the pressure-dependent quantities in the affected region.

7.2. *Code Timings*

We conducted additional computations of the problem described above on a Cray C90 in order to examine in detail the computational cost of our method. In our implementation we have taken care to ensure that every loop that could vectorize on the Cray does. We studied two cases, a single 100×100 grid on which refinement is not allowed, and the same case but using AMR to achieve effective 400×400 resolution. At CFL 0.4 the 100×100 case ran for 308 time steps while the effective 400×400 case ran for 318 time steps to reach time $t = 1.3$ μs from the start of the computation. (The initial conditions were such that the shock struck the Mo/Morb interface at time $t = 469$ ns.)

In all of the runs we determined the average cost of integrating one cell for one time step was consistently 20.7 μs of Cray C90 CPU time. This figure includes the cost of setting up the sweep arrays and of all calls to the EOS routines, the Riemann problem solver, and other steps in the second-order Godunov method, but it *excludes* the cost of reconstructing the interface from volume fraction data. We present per-cell data excluding the interface routines since these routines are not currently written to optimize the speed of the algorithm. When we included the cost of the interface reconstruction routines, the average cost per cell increased by about 12 μs of CPU time.

The *total* cost to advance the entire grid with an *effective* 400×400 resolution by one time step is about 6.99 CPU, including AMR overhead but still excluding interface reconstruction. The *total* cost to advance a *real* 400×400 grid one time step is calculated to be $400^2 \times 4 \times 20.7 \times$

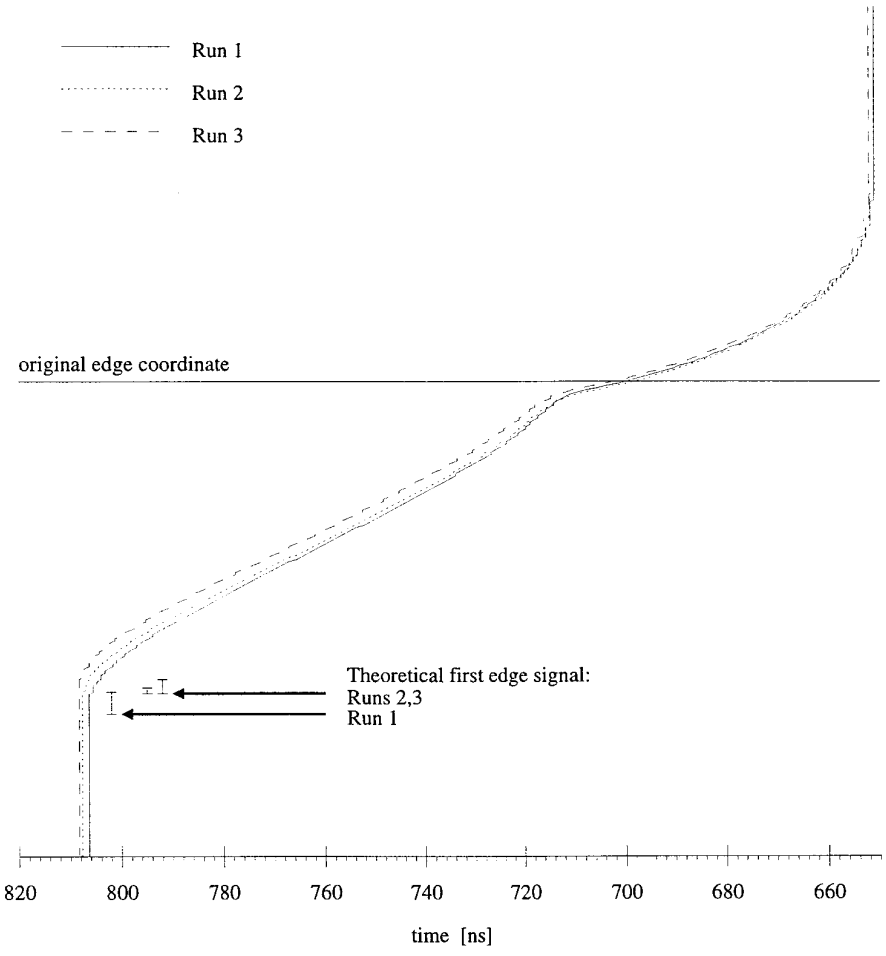

FIG. 15. Synthetic streak records with nominal and perturbed MORB parameters. Run 1 (solid line) is an experimentally determined parameter set; run 2 (dotted line) is the sound speed reduced by increasing γ_0; and run 3 (dashed line) is the sound speed reduced to the same level as run 2 by decreasing q. The error bars indicate the difference between the theoretical first observation of edge effects (indicated by arrows) and their first observation in the synthetic streak record. The synthetic records shown here have resolution similar to that of experimental records.

10^{-6} = 13.25 CPU-s, (400^2 cells, and 4 fine time steps per coarse time step, at 20.7 $\times$ 10^{-6} s per cell). Based on this scaling, employing AMR to achieve high resolution reduces the computational expense by 6.26 CPU-s, per time step, or 47%, in the example given.

8. CONCLUSIONS

We have presented a new numerical algorithm for the integration of the Euler equations in multiphase systems in which each of the phases is modeled by a Mie–Grüneisen EOS. In our algorithm we solve a conservation equation for the mass and energy of each material phase, a transport equation for the volume fraction of each phase, and an equation that represents the conservation of momentum for the multiphase composite. The fundamental assumption underlying this approximation is that in a cell that contains more than one phase, the pressure and velocity of the composite are single valued, but the specific volume and other thermodynamic properties of each phase are separate. The resulting system of conservation laws is hyperbolic and can be solved with modern numerical techniques for approximating solutions of hyperbolic conservation laws.

We use a second-order Godunov method to determine the time- and edge-centered fluxes of conserved quantities, which we then advance in time using a standard conservative finite difference update. At multiphase edges the Godunov fluxes are determined by solving the Riemann problem for an effective single phase whose properties are those of the multiphase composite and then determining the advected volumes of each component phase using a second-order volume-of-fluid interface reconstruction algorithm. An equilibration step readjusts the volume fractions

of the individual phases to enforce the condition of isotropic stress within individual computational cells.

Our algorithm for modeling multiple phases is based on an algorithm due to Colella *et al.* [15]. It differs from their algorithm principally in details related to the underlying EOS model. For instance, with our EOS model a linearization based on constant isentropic bulk modulus K_S is reasonable. However, for ideal gases where

$$K_S = P\Gamma \tag{8.1}$$

an assumption of constant polytropic index Γ is more appropriate. Moreover, our method permits states with nonpositive pressures and zero densities, and such states are incompatible with the ideal gas EOS.

Our one-dimensional integrator is part of an operator-split two-dimensional integrator embedded within an adaptive mesh refinement shell. Details of the AMR algorithm that are specific to our implementation are described. The use of AMR allows us to focus the majority of the computational cost on those parts of the problem domain that we deem to be interesting. We have chosen to concentrate the computational effort on three regions: interfaces between phases, regions of large absolute divergence (shocks and steep rarefactions), and regions with comparatively large errors in density as judged by using Richardson extrapolation to estimate the local truncation error in the computed density.

We have used this method to study wave interactions in laboratory experiments designed to measure the equation of state of liquid silicates [35]. Here we have presented additional computations aimed at extracting new information from the experiments described in that paper. The computations began with a 100×100 computational grid, with interfaces, strong waves, and error-prone regions selected for refinement on an effective 400×400 computational grid. We computed synthetic streak records with spatial and temporal accuracy comparable to laboratory data. These synthetic streak records suggest that inferences of the high-pressure sound speed within the shocked liquid are subject to systematic underestimation because of the weakness of the edge effect at its leading edge. Also, the structure of the affected signal cannot be used to deduce the pressure dependence of the liquid sound speed in a single experiment.

APPENDIX: AN "EXACT" MULTIPHASE RIEMANN SOLVER

In essence, an "exact" multiphase Riemann solver consists of the integral equations (3.5), but where all individual phase thermodynamic terms are replaced by their effective single-phase counterparts (i.e., $\overline{\rho}$ for ρ, etc). Hugoniots constructed in this manner, which is sometimes called "the method of mixtures" [31, 32], have proven successful in predicting the shock properties of alloys and binary mechanical mixtures of metals.

Of those bulk composite properties needed, only the Grüneisen parameter has not yet been specified. The simplest model for the thermodynamic Grüneisen parameter of the composite is obtained by assuming that during isopycnic compression: (1) the phases remain under isotropic stress, (2) no energy is exchanged between phases, and (3) the individual phase densities remain constant. Under these conditions,

$$(\overline{\rho}\overline{\gamma})^{-1} = \left.\frac{\partial \overline{E}}{\partial P}\right|_{\overline{\rho}} = \sum_{\alpha} \frac{f^{\alpha}\rho^{\alpha}}{\overline{\rho}} \left.\frac{\partial E^{\alpha}}{\partial P}\right|_{\rho^{\alpha}},$$

whence

$$\overline{\gamma} = \left(\sum_{\alpha} f^{\alpha}/\gamma^{\alpha}\right)^{-1}.$$

In constructing the effective single-phase bulk modulus we assumed that during isentropic compression the entropies of the individual phases remain constant. The self-consistent isentropic expansion of a binary composite is thus

$$\left.\frac{\partial}{\partial P}\right|_{S} \begin{pmatrix} u \\ \overline{\rho} \\ \overline{E} \\ \rho^1 \\ E^1 \\ \rho^2 \\ E^2 \end{pmatrix} = \begin{pmatrix} \sqrt{\overline{V}/\overline{K}_S} \\ \overline{\rho}/\overline{K}_S \\ P\overline{V}/\overline{K}_S \\ \rho^1/K_S^1 \\ PV^1/K_S^1 \\ \rho^2/K_S^2 \\ PV^2/K_S^2 \end{pmatrix}. \tag{A.1}$$

We can envision the shock compression process as consisting of an isentropic compression, followed by an isopycnic energy change. Thus for each differential change in pressure on the Hugoniot $\delta P_{\mathscr{H}}$ there is an isopycnic pressure change of

$$\delta P_{\overline{\rho}} = \frac{\partial P}{\partial \overline{S}}\bigg|_{\overline{\rho}} \frac{\partial \overline{S}}{\partial P}\bigg|_{\mathscr{H}} \delta P_{\mathscr{H}} = \overline{\rho}\overline{\gamma} \frac{\overline{K}_S(\overline{V}_0 - \overline{V}) - \overline{V}(P - P_0)}{2\overline{K}_S - \overline{\gamma}(P - P_0)} \delta P_{\mathscr{H}},$$

and a corresponding isentropic part

$$\delta P_{\overline{S}} = \frac{\overline{K}_S}{\overline{K}_{\mathscr{H}}} \delta P_{\mathscr{H}} = \overline{\rho}\overline{K}_S \frac{2\overline{V} - \overline{\gamma}(\overline{V}_0 - \overline{V})}{2\overline{K}_S - \overline{\gamma}(P - P_0)} \delta P_{\mathscr{H}},$$

where $\overline{V}_0$ and P_0 are at the mixed phase Hugoniot centering

point and $\delta P_{\overline{S}} + \delta P_{\overline{\rho}} = \delta P_{\mathscr{H}}$. Now we divide the total differential pressure change into component isopycnic and isentropic parts. During the isopycnic process the assumptions described above in the derivation of $\overline{\gamma}$ hold, and during the isentropic part entropies are individually held constant. The self-consistent shock properties of a binary composite are thus

$$\left.\frac{\partial}{\partial P}\right|_{\mathscr{H}} \begin{pmatrix} \overline{\rho} \\ \overline{E} \\ \rho^1 \\ E^1 \\ \rho^2 \\ E^2 \end{pmatrix} = \begin{pmatrix} \overline{\rho}/\overline{K}_{\mathscr{H}} \\ \tfrac{1}{2}(\overline{V}_0 - \overline{V} + (P + P_0)\overline{V}/\overline{K}_{\mathscr{H}}) \\ (\rho^1/K_S^1)\delta P_{\overline{S}}/\delta P_{\mathscr{H}} \\ (PV^1/K_S^1)\delta P_{\overline{S}}/\delta P_{\mathscr{H}} + (V^1/\gamma^1)\delta P_{\overline{\rho}}/\delta P_{\mathscr{H}} \\ (\rho^2/K_S^2)\delta P_{\overline{S}}/\delta P_{\mathscr{H}} \\ (PV^2/K_S^2)\delta P_{\overline{S}}/\delta P_{\mathscr{H}} + (V^2/\gamma^2)\delta P_{\overline{\rho}}/\delta P_{\mathscr{H}} \end{pmatrix}. \tag{A.2}$$

The particle velocity may be determined directly from the Rankine–Hugoniot jump relations,

$$u = \sqrt{(P - P_0)(\overline{V}_0 - \overline{V})},$$

instead of by integration.

An ''exact'' multiphase Riemann solver may be constructed as described in Section 3, but by integrating the vector equations (A.1) and (A.2) to the pressure where the L and R integrals converge to a common velocity. The integrals then provide the individual phase ''*'' properties needed for the construction of individual phase fluxes.

ACKNOWLEDGMENTS

We thank P. Colella, H. Glaz, and R. Ferguson for sharing their unpublished manuscript with us and for many helpful discussions. We also thank John Bell, Marsha Berger, Jeff Saltzman, and Mike Welcome for providing us with a copy of their 2D FORTRAN Adaptive Mesh Refinement code.

REFERENCES

1. A. M. Abd-el-Fattah and L. F. Henderson, *J. Fluid Mech.* **86,** 15 (1978).
2. A. M. Abd-el-Fattah and L. F. Henderson, *J. Fluid Mech.* **89,** 79 (1978).
3. A. M. Abd-el-Fattah, L. F. Henderson, and A. Lozzi, *J. Fluid Mech.* **76,** 157 (1976).
4. J. Abdallah, G. I. Kerley, B. I. Bennett, J. D. Johnson, R. C. Albers, and W. F. Huebner, *HYDSES*: *A Subroutine Package for Using SESAME in Hydrodynamic Codes*, Tech. Rep. LA-8209-MS (Los Alamos National Laboratory, Los Alamos, NM, 1980).
5. F. L. Addessio, D. E. Carroll, J. K. Dukowicz, F. H. Harlow, J. N. Johnson, B. A. Kashiwa, M. E. Maltrud, and H. E. Rupple, *CAVEAT*: *A Computer Code for Fluid Dynamics Problems with Large Distortion and Internal Slip*, Tech. Rep. LA-10613-MS (Los Alamos National Laboratory, Los Alamos, NM, 1986).
6. L. V. Al'tshuler, S. B. Kormer, M. I. Brazhnik, L. A. Vladimirov, M. P. Speraanskaya, and A. I. Funtikov, *Sov. Phys. JETP* **11,** 766 (1960).
7. J. Bell, M. Berger, J. Saltzman, and M. Welcome, *SIAM J. Sci. Comput.* **15,** 127 (1994).
8. M. J. Berger and P. Colella. *J. Comput. Phys.* **82,** 64 (1989).
9. M. J. Berger and J. Oliger, *J. Comput. Phys.* **53,** 484 (1984).
10. M. J. Berger and I. Rigoutsos, *IEEE Trans. Systems*, *Man Cybernet.* **21,** 1278 (1991).
11. H. B. Callen, *Thermodynamics and an Introduction to Thermostatistics*, 2nd ed. (Wiley, New York, 1985).
12. P. Colella, *SIAM J. Sci. Stat. Comput.* **6,** 104 (1985).
13. P. Colella, *J. Comput. Phys.* **87,** 171 (1990).
14. P. Colella and H. M. Glaz, *J. Comput. Phys.* **59,** 264 (1985).
15. P. Colella, H. M. Glaz, and R. E. Ferguson, Multifluid algorithms for Eulerian finite difference methods, manuscript, 1996.
16. P. Colella, L. F. Henderson, and E. G. Puckett, in *Proceedings of the AIAA 9th Computational Fluid Dynamics Conference*, Article Number AIAA-89-1973 (AIAA, Buffalo, NY, 1989). p. 426.
17. P. Colella and P. R. Woodward, *J. Comput. Phys.* **54,** 174 (1984).
18. T. S. Duffy and T. J. Ahrens, *Geophys. Res. Lett.* **21,** 473 (1994).
19. J. K. Dukowicz, *J. Comput. Phys.* **61,** 119 (1985).
20. H. M. Glaz, P. Colella, I. I. Glass, and R. L. Deschambault, *Proc. R. Soc. London Ser. A* **398,** 117 (1985).
21. S. K. Godunov, *Mat. Sb.* 271 (1959); translation, Cornell Aeronautical Laboratory.
22. L. F. Henderson, P. Colella, and E. G. Puckett, *J. Fluid Mech.* **224,** 1 (1991).
23. K. S. Holian, *T-4 Handbook of Material Properties Data Bases*, Tech. Rep. LA-10160-MS (Los Alamos National Laboratory, Los Alamos, NM, 1984).
24. R. G. Jahn, *J. Fluid Mech.* **1,** 457 (1956).
25. J. E. Pilliod Jr. and E. G. Puckett, Second-order volume-of-fluid algorithms for tracking material interfaces, manuscript in preparation (1996).
26. A. Lapidus, *J. Comput. Phys.* **2,** 154 (1967).
27. R. J. LeVeque, *Numerical Methods for Conservation Laws*, (Birkhäuser, Basel, 1990).
28. S. P. Marsh, *LASL Shock Hugoniot Data*, (University of California Press, Berkeley, 1980).
29. J. M. McGlaun, S. L. Thompson, C. N. Kmetyk, and M. G. Elrick, *A Brief Description of the Three Dimensional Shock Wave Physics Code CTH*, tech. rep. (Sandia National Laboratory, 1992).
30. J. M. McGlaun and P. Yarrington. Large deformation wave codes, in *High-Pressure Shock Compression of Solids*, edited by J. R. Asay and M. Shahinpoor, (Springer-Verlag, New York, 1993), p. 323.
31. R. G. McQueen, Shock waves in condensed media: Their properties and the equation of state of materials derived from them, in *High-Pressure Equations of State*: *Theory and Applications*, edited by S. Eliezer and R. A. Ricci (North-Holland, New York, 1991), p. 101.
32. R. G. McQueen, S. P. Marsh, J. W. Taylor, J. N. Fritz, and W. J. Carter, The equation of state of solids from shock wave studies, in *High-Velocity Impact Phenomena,* edited by R. Kinslow (Academic Press, New York, 1970), p. 293.
33. R. Menikoff and B. J. Plohr. *Rev. Mod. Phys.* **61**(1), 75 (1989).
34. G. H. Miller and T. J. Ahrens, *J. Appl. Phys.* **63,** 4469 (1988).

35. G. H. Miller and E. G. Puckett, *J. Appl. Phys.* **75,** 1426 (1994).
36. G. H. Miller, E. M. Stolper, and T. J. Ahrens, *J. Geophys. Res.* **96,** 11,831 (1991).
37. F. D. Murnaghan, *Finite Deformation of an Elastic Solid* (Dover, New York, 1967).
38. E. G. Puckett, L. F. Henderson, and P. Colella, submitted for publication.
39. E. G. Puckett and G. H. Miller, The numerical computation of high-velocity impact phenomena, in *Proceedings of the 20th International Symposium on Shock Waves*, *California Institute of Technology*, *July 1995* edited by H. Hornung (Springer-Verlag, New York/Berlin, to appear).
40. L. R. Rowan, I. *Equation of State of Molten Mid-Ocean Ridge Basalt*; II. *Structure of Kilauea Volcano*, Ph.D. thesis (California Institute of Technology, January 1993).
41. L. R. Rowan, T. J. Ahrens, and E. M. Stolper. *EOS Trans. Amer. Geophys. Union* **72,** 548 (1991) [abstract].
42. G. Strang, *Numer. Math.* **6,** 37 (1964).
43. S. L. Thompson and H. S. Lauson, *Improvements in the CHART-D Radiation-Hydrodynamic Code*. III. *Revised Analytic Equations of State*, Tech. Rep. SC-RR-71 0714, (Sandia National Laboratory, Albuquerque, NM, 1972).
44. J. A. Trangenstein and P. Colella, *Comm. Pure Appl. Math.* **44,** 41 (1991).
45. B. van Leer, *J. Comput. Phys.* **32,** 101 (1979).
46. J. M. Walsh, R. G. Shreffler, and F. J. Willig, *J. Appl. Phys.* **24**(3), 349 (1953).
47. F. Wang, J. Glimm, J. Grove, B. J. Plohr, and D. Sharp, *Impact Comput. Sci. Engrg.* **5,** 285 (1993).
48. M. L. Wilkins, in *Methods in Computational Physics*, edited by B. Alder, S. Fernbach, and M. Rotenberg, Vol. 3, p. 211 (Academic Press, New York, 1964).
49. P. Woodward and P. Colella, *J. Comput. Phys.* **54,** 115 (1984).
50. J. A. Zukas, Survey of computer codes for impact simulation, in *High Velocity Impact Dynamics*, edited by Jonas A. Zukas, (Wiley, New York, 1990), p. 593.